Insights into ENSO Diversity from an Intermediate Coupled Model. Part II: Role of Nonlinear Dynamics and Stochastic Forcing

LICHENG GENG[a] AND FEI-FEI JIN[a]

[a] *Department of Atmospheric Sciences, School of Ocean and Earth Science and Technology, Honolulu, Hawaii*

(Manuscript received 22 January 2023, in final form 5 June 2023, accepted 28 July 2023)

ABSTRACT: In this study, we investigate how a single leading linear El Niño–Southern Oscillation (ENSO) mode, as studied in Part I, leads to the irregular coexistence of central Pacific (CP) and eastern Pacific (EP) ENSO, a phenomenon known as ENSO spatiotemporal diversity. This diversity is fundamentally generated by deterministic nonlinear pathways to chaos via the period-doubling route and, more prevailingly, the subharmonic resonance route with the presence of a seasonally varying basic state. When residing in the weakly nonlinear regime, the coupled system sustains a weak periodic oscillation with a mixed CP/EP pattern as captured by the linear ENSO mode. With a stronger nonlinearity effect, the ENSO behavior experiences a period-doubling bifurcation. The single ENSO orbit splits into coexisting CP-like and EP-like ENSO orbits. A sequence of period-doubling bifurcation results in an aperiodic oscillation featuring irregular CP and EP ENSO occurrences. The overlapping of subharmonic resonances between ENSO and the seasonal cycle allows this ENSO irregularity and diversity to be more readily excited. In the strongly nonlinear regime, the coupled system is dominated by regular EP ENSO. The deterministic ENSO spatiotemporal diversity is thus confined to a relatively narrow range corresponding to a moderately unstable ENSO mode. Stochastic forcing broadens this range and allows ENSO diversity to occur when the ENSO mode is weakly subcritical. A close relationship among a weakened mean zonal temperature gradient, stronger ENSO activity, and more (fewer) occurrences of EP (CP) ENSO is noted, indicating that ENSO–mean state interaction may yield ENSO regime modulations on the multidecadal time scale.

KEYWORDS: Decadal variability; ENSO; Idealized models; Nonlinear dynamics; Stability

1. Introduction

El Niño–Southern Oscillation (ENSO) is an influential natural phenomenon for Earth's ecosystem and human society due to its far-reaching environmental and societal impacts across the globe. In contrast to the canonical ENSO that features a maximum sea surface temperature anomaly (SSTA) in the eastern Pacific (EP), another type of ENSO with a warm SSTA located in the central Pacific (CP) has seen more occurrences in recent decades (Lee and McPhaden 2010; Chung and Li 2013; Xiang et al. 2013; Freund et al. 2019). Corresponding to the contrasting spatial pattern and magnitude of the associated SSTA, the two types of ENSO exhibit substantial differences in their impacts [see reviews by Yeh et al. (2014), Capotondi et al. (2015), Yang et al. (2018), and Taschetto et al. (2020)]. The existence of two types of ENSO is typically referred to as ENSO diversity. To avoid ambiguity, the terminology "two types of ENSO" in this paper shall not be interpreted as being different from "two types of El Niño," considering that La Niña does not exhibit significant pattern diversity (Kug and Ham 2011; Taschetto et al. 2014).

Process-oriented studies confirmed the distinct growing and turnabout mechanisms associated with the two types of ENSO (Kug et al. 2009, 2010; McPhaden 2012; Capotondi 2013; Ren and Jin 2013). However, the fundamental mechanism for ENSO diversity has not yet been completely understood. A definite answer to this question not only promotes our basic understanding of the observed ENSO diversity but also benefits the modeling community in terms of improving model performance in simulating ENSO diversity. Several potential building blocks for understanding the coexistence of EP and CP ENSO have been proposed, including modal growth from two dominant linear ENSO-like modes resembling the two types of ENSO (Bejarano and Jin 2008; Xie and Jin 2018); noise-driven nonmodal growth of the two types of ENSO from their respective optimal initial perturbations (Newman et al. 2011a,b; Vimont et al. 2014, 2022; Capotondi and Sardeshmukh 2015); the role of convective heating threshold in leading to an EP-like nonlinear manifestation of ENSO (Takahashi and Dewitte 2016); and effects of state-dependent westerly wind burst (WWB) events (Chen et al. 2015; Chen and Majda 2017; Hayashi and Watanabe 2017; Chen et al. 2018; Yang et al. 2021). In Part I of this two-part study (Geng and Jin 2023, hereafter Part I), we identified the existence of a single leading ENSO mode in the Cane–Zebiak-type framework (Zebiak and Cane 1987). This finding precludes the possibility that the two types of ENSO simulated in the Cane–Zebiak-type model, such as in Bejarano and Jin (2008), Chen et al. (2015), Hayashi and Watanabe (2017) and Xie and Jin (2018), are randomly excited from two coexisting leading ENSO modes. In addition, we demonstrated that stochastic forcing is insufficient to lead to irregular alternation between the two types of ENSO characterizing the observed ENSO diversity via linear processes, even with the presence of low-frequency climate variability. Therefore, it is logical to speculate that nonlinear processes may play an important role in ENSO diversity.

The effects of nonlinear processes on complex ENSO behavior are widely acknowledged. With a low-order model, Timmermann et al. (2003) suggested that strong nonlinearity

Corresponding author: Fei-Fei Jin, jff@hawaii.edu

DOI: 10.1175/JCLI-D-23-0044.1

© 2023 American Meteorological Society. This published article is licensed under the terms of the default AMS reuse license. For information regarding reuse of this content and general copyright information, consult the AMS Copyright Policy (www.ametsoc.org/PUBSReuseLicenses).

Brought to you by University of Hawaii at Manoa, Library | Unauthenticated | Downloaded 10/03/23 09:00 AM UTC

could lead to ENSO bursting behavior. Nonlinearity also plays a key role in the El Niño–La Niña amplitude and duration asymmetry (e.g., Kang and Kug 2002; An and Jin 2004; Ohba and Ueda 2009; Su et al. 2010; DiNezio and Deser 2014; Chen et al. 2016). The convective heating nonlinearity has been suggested as a relevant nonlinear process for ENSO bimodality and diversity (Takahashi and Dewitte 2016; Williams and Patricola 2018; Okumura 2019; Takahashi et al. 2019; Geng et al. 2020). As deep convection is preferably excited over warm SST exceeding the convective threshold (Graham and Barnett 1987), EP El Niño can only survive with substantial warm SSTA in the eastern Pacific. The ENSO–WWB interaction serves as another source of atmospheric nonlinearity as WWB occurs more frequently and farther eastward with larger SSTA in the central-eastern Pacific (Eisenman et al. 2005; Tziperman and Yu 2007; Seiki and Takayabu 2007; Puy et al. 2016). With an extended recharge oscillator (RO) model incorporating convective heating nonlinearity, Takahashi et al. (2019) successfully reproduced ENSO bimodality. The relevance of such atmospheric nonlinearity to ENSO diversity, however, needs to be further investigated with a more complex model that resolves varying ENSO spatial patterns.

Some previous attempts at modeling ENSO diversity with idealized models demonstrated the key role of WWB, without which the simulated ENSO exhibits regular oscillations (Chen et al. 2015; Chen and Majda 2017). However, it may not be accurate to simply attribute the simulated ENSO diversity to WWB without examining the effects of deterministic nonlinearity. Using a deterministic intermediate model, Münnich et al. (1991) noted that with increasing thermocline feedback, the coupled system experiences the "route to chaos" comprising a Hopf bifurcation from an at-rest steady state to a periodic orbit, a second bifurcation to a period doubling, and a third bifurcation to aperiodic behavior. Such a deterministic route to chaos was then further suggested to be relevant to ENSO irregularity when the ENSO–seasonal cycle interaction is taken into consideration (Jin et al. 1994; Tziperman et al. 1994; Chang et al. 1996). Inspired by these studies, further investigation is needed to determine whether ENSO diversity survives in a nonlinear simulation without stochastic forcing.

Multiple ENSO flavors were successfully reproduced in several modeling studies with the Cane–Zebiak-type models (e.g., Chen et al. 2015; Hayashi and Watanabe 2017; Geng and Jin 2022, hereafter GJ22). Part I clearly demonstrated that only one leading ENSO mode is allowed by the Cane–Zebiak-type framework. In this paper, we aim to reveal how this ENSO mode evolves into ENSO diversity. As in Part I, the revised Cane–Zebiak model (RCZ hereafter) developed in GJ22 serves as the research tool for this study. The key processes involved are examined through a hierarchical modeling approach with RCZ. In section 2, a brief overview of ENSO diversity simulated in RCZ under the observed climate condition is presented. Section 3 compares the ENSO behavior in situations where the efficiency of nonlinear processes gradually increases. This allows careful investigation of the effect of deterministic nonlinearity on ENSO diversity. Further comparison of ENSO behavior in simulations where stochastic forcing is switched on or off allows us to study how the stochastic processes contribute to ENSO diversity. Section 4 investigates the ENSO–mean state interaction in the context of ENSO diversity. A summary and some discussions are provided in section 5.

2. ENSO diversity in RCZ under the observed climate condition

Under the observed climate condition that involves the observed mean state and model parameters, GJ22 demonstrated that RCZ successfully simulates ENSO diversity, featuring irregular occurrences of EP and CP El Niño events. As introduced in Part I, a few minor modifications were made to the model formulation of RCZ in this study compared with GJ22. In this section, we briefly revisit the RCZ-simulated ENSO behavior in a long-term simulation under the observed climate condition. As will be discussed later, the features of ENSO diversity barely change from GJ22. The model is prescribed with either a seasonally varying or an annual mean basic state obtained from the long-term average of observations. By allowing the seasonal modulation of the feedback processes via using a seasonally varying basic state, the effect of background seasonal cycle would be included. The total length of the simulation is 1100 years, and the first 100 years of data are omitted for the purpose of removing the spinup stage. The long-term average is removed from all the model outputs prior to analysis. The simulation is subject to stochastic zonal surface wind stress forcing mimicking the observed WWB events. Zonal surface wind associated with stochastic forcing is in the form of $u_{stc}(x, y, t) = I_{stc}P(t)u_0 \exp\{-[(x - x_0)^2/\Delta x^2] - [(y - y_0)^2/\Delta y^2]\}$, where $u_0 = 6.5$ m s^{-1}, $\Delta x = 20°$, $\Delta y = 6°$, and $y_0 = 0°$. The term x_0 is the center longitude of the WWB, and it depends on the ENSO state; $P(t)$ represents a stochastic process and controls the occurrence of the WWB. More details on the formulation of x_0 and $P(t)$ can be found in GJ22 (see their supplemental material). Here, a nondimensional coefficient I_{stc} is introduced to control the relative intensity of stochastic forcing. It has a default value of 1 and will be varied in section 3c to investigate how the intensity of stochastic forcing affects ENSO behavior.

The time evolution of equatorial SSTA during a 50-yr segment of the 1000-yr simulation with a seasonally varying basic state is shown in Fig. 1a. The most salient feature of Fig. 1a is the significant interevent difference in the SSTA pattern associated with the warm events. Both CP El Niño (e.g., years 15, 25, 31, 40, and 42) and EP El Niño (e.g., years 1, 22, and 47) events are identified. Consistent with the observations, CP El Niño is of smaller amplitude than EP El Niño. Some other El Niño events (e.g., years 4, 19, and 44) exhibit a broad SSTA center in the central-eastern Pacific and exhibit similar amplitudes of SSTA averaged over the CP and EP region. These events resemble the observed mixed CP/EP events but are not clearly distinguished from the CP events.

For subjective categorization, all El Niño events are first identified according to the criteria that the Niño-3, Niño-4, or Niño-3.4 index exceeds 0.5°C for five consecutive overlapping seasons. Note that the following results are not qualitatively

Brought to you by University of Hawaii at Manoa, Library | Unauthenticated | Downloaded 10/03/23 09:00 AM UTC

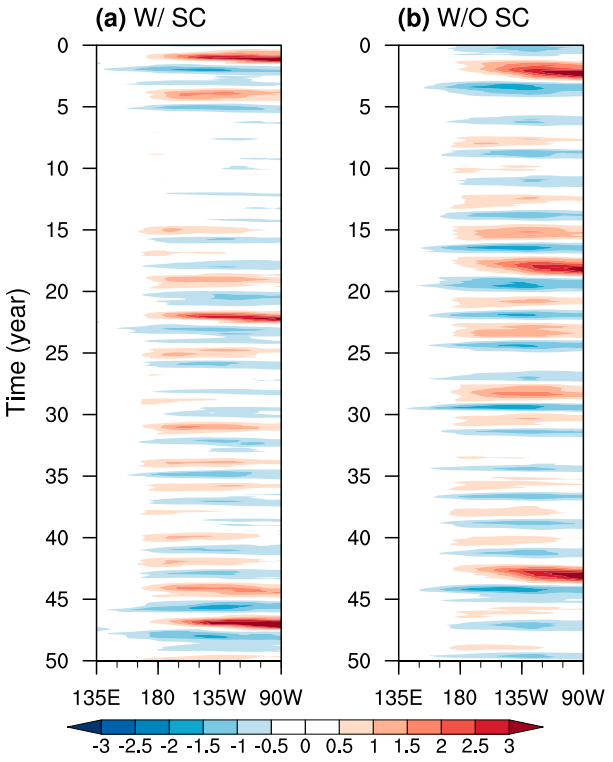

FIG. 1. 50-yr time evolution of equatorial (5°S–5°N average) SSTA (°C) in stochastic simulations with default model parameters. The simulations are subject to (a) a seasonally varying basic state and (b) an annual mean basic state.

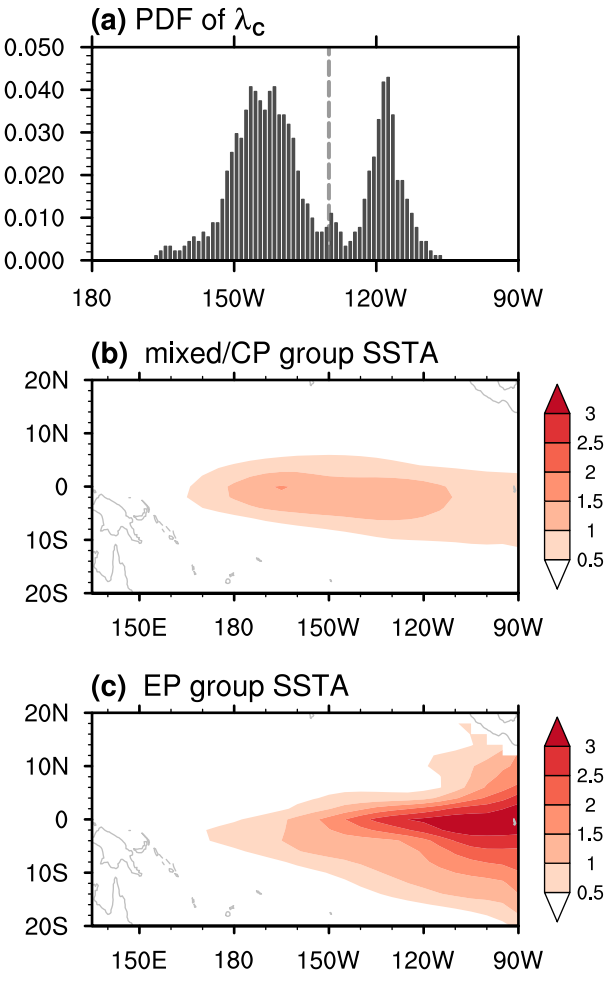

FIG. 2. (a) The probability density function (PDF) of the equatorial SSTA centroid longitude λ_C at the peak phase of El Niño events. The PDF is estimated based on binned histograms from the 1000-yr simulation. The width of the bins is 1° in longitude. The vertical dashed line marks the longitude at 130°W. (b) Composite of SSTA pattern (°C) at the peak phase of El Niño events in the mixed/CP group. (c) As in (b), but for the composite in the EP group. See the text for the criteria of El Niño categorization. The prescribed basic state of this simulation includes a seasonal cycle.

sensitive to the identification criteria. We then calculate the centroid longitude of SSTA at the peak phase of each El Niño event. The centroid longitude λ_c is defined as $\lambda_c = \int_{\lambda_W}^{\lambda_E} \lambda T_e d\lambda / \int_{\lambda_W}^{\lambda_E} T_e d\lambda$, where λ is the longitude, T_e is equatorial SSTA meridionally averaged between 5°S and 5°N, $\lambda_W = 140°$E, and $\lambda_E = 90°$W. Only positive T_e is utilized to calculate λ_c. During the peak phase of El Niño, positive T_e dominates over the equatorial Pacific. As shown in Fig. 2a, the probability density function (PDF) of the λ_c associated with all the El Niño events clearly exhibits two discrete peaks, suggesting the bimodal nature of El Niño. According to Fig. 2a, we classify the El Niño events into two groups where λ_c is located either to the west or east of 130°W. The composited SSTA patterns at the peak phase for these two groups are clearly distinguished (Figs. 2b,c). The former group is reminiscent of the observed CP El Niño as it sees a weak center in the CP region. However, in comparison with the observations (e.g., Kug et al. 2009), the SSTA pattern in this group extends more eastward. The SSTA pattern being eastward extended is attributed to the fact that both mixed CP/EP and CP El Niño events are included in this group. Thus, we refer to this group of El Niño as the "mixed/CP group." The second group of El Niño exhibits maximum SSTA in the EP region and is thus called the "EP group." As will be discussed later, the difference between mixed CP/EP El Niño and CP El Niño is much less than their difference with EP El Niño in terms of the dynamical mechanism. This lends support to our categorization of El Niño into two groups.

We also performed a long-term simulation with an annual mean basic state. As shown in Fig. 1b, the pattern diversity associated with El Niño can still be identified in this scenario. Compared with that observed with a seasonally varying basic state, the simulated ENSO behavior in this case does not exhibit much difference, except that there are slightly more (fewer) occurrences of mixed CP/EP (CP) El Niño events.

In addition to ENSO's pattern diversity, another interesting feature shown in Fig. 1a is that, as typically found in observations, the EP El Niño–like events are followed by prolonged multiyear La Niña or double-dip La Niña. Such phenomenon of multiyear La Niña following strong EP-like El Niño has

Brought to you by University of Hawaii at Manoa, Library | Unauthenticated | Downloaded 10/03/23 09:00 AM UTC

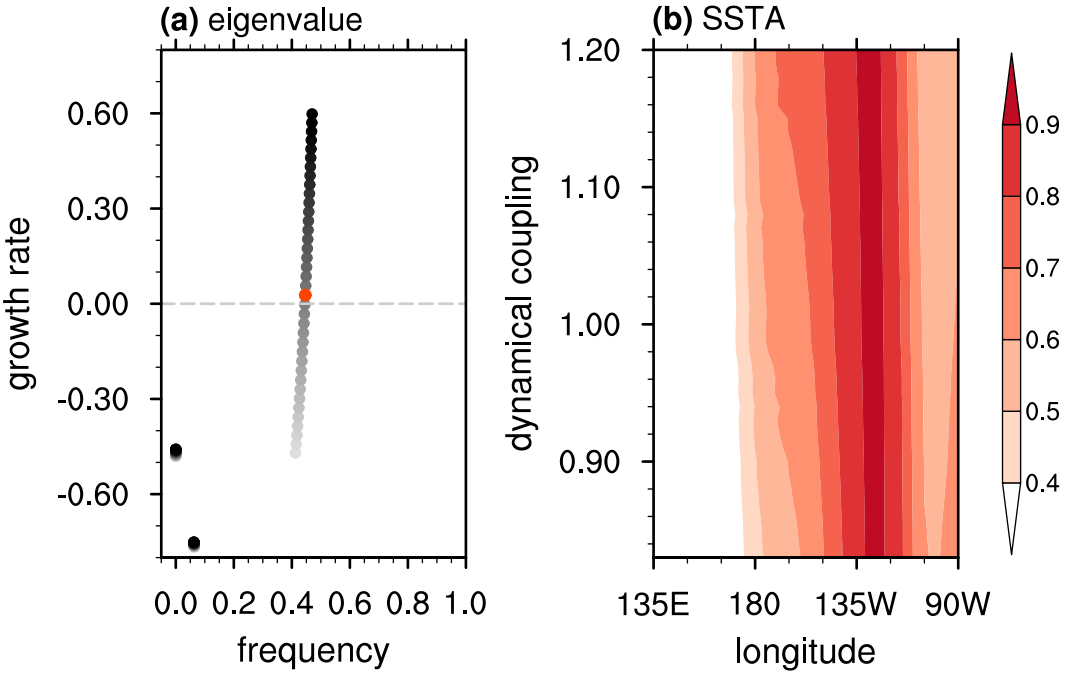

FIG. 3. (a) Growth rate (yr^{-1}) and frequency (yr^{-1}) of RCZ's eigenmodes obtained with a series of linear stability analyses in which the dynamical coupling coefficient varies from 0.82 to 1.2 with an increment of 0.01. The linear stability analyses are performed with an annual mean basic state. The colors of the dots denote the values of the dynamical coupling coefficient, with lighter (darker) dots corresponding to weaker (stronger) dynamical coupling. The red dot marks the ENSO mode (i.e., the first coupled mode) obtained with the dynamical coupling coefficient at its default value of 1. (b) Dependence of the normalized equatorial SSTA (°C) associated with the ENSO mode at its warm peak phase on the dynamical coupling coefficient.

also been identified in the observations and climate model simulations (e.g., Iwakiri and Watanabe 2021). With an annual mean basic state, however, this kind of El Niño/La Niña duration asymmetry is less obvious. The underlying physics for the role of the seasonal cycle in multiyear La Niña deserves further investigation.

3. Pathway from the ENSO mode toward ENSO diversity

In Part I, we demonstrated that there is a single linear ENSO mode in the Cane–Zebiak-type framework. With the annual mean basic state, this ENSO mode is of near-neutrality, has a period of about 27 months, and features in situ SSTA growth and decay centering in the central-eastern Pacific. In this section, we explore how such a single ENSO mode leads to multiple ENSO flavors in the long-term simulation as discussed in section 2. It can be logically speculated that the nonlinear and stochastic processes present in the long-term simulation but missing in the linear stability analysis may play an important role. Although the linear stochastic simulations shown in Part I do not exhibit the coexistence of multiple ENSO flavors, the possibility that stochastic forcing favors ENSO diversity through the nonlinear dynamics cannot be ruled out. In this section, we examine whether and how the nonlinear processes and stochastic forcing pave the pathway from the ENSO mode toward ENSO diversity.

a. Role of deterministic nonlinearity with an annual mean basic state

To isolate the effects of nonlinear processes on ENSO diversity, we perform deterministic simulations without stochastic forcing. A series of simulations with nonlinearity smoothly switched on allows scrutiny of the effects of nonlinear processes. This is technically accomplished via varying the dynamical coupling coefficient μ, which controls the magnitude of wind stress response to SSTA forcing (see section 3 in Part I). The dynamical coupling coefficient has a default value of 1 and it varies from 0.82 to 1.2 with an increment of 0.01 to yield thirty-nine 1000-yr simulations. All other model parameters are at their default values. To filter out the impact of ENSO–seasonal cycle interaction, an annual mean basic state is used. This allows a direct comparison between the linear stability analysis and long-term simulation and thus benefits investigating how nonlinear processes take effect. As indicated in Fig. 3, an ENSO-like linear mode is identified as the first leading mode across the above choices of μ. This ENSO mode's frequency and spatial pattern exhibit little sensitivity to μ. It has a period of about 2 years and the maximum SSTA during its peak phase is located in the central-eastern Pacific. On the other hand,

Brought to you by University of Hawaii at Manoa, Library | Unauthenticated | Downloaded 10/03/23 09:00 AM UTC

the growth rate of the ENSO mode increases from about $-0.5\ \mathrm{yr}^{-1}$ to about $0.6\ \mathrm{yr}^{-1}$ with increasing μ. In the subcritical (supercritical) regime where the ENSO mode is stable (unstable), nonlinear processes are expected to play a minor (nonnegligible) role. For this reason, this series of simulations provides a testbed to investigate the nonlinearity effect by examining the ENSO behavior across the subcritical and supercritical ENSO mode regimes.

How the amplitude of SSTA variability, measured by the standard deviation of equatorial SSTA, varies with increasing μ in long-term simulations is illustrated in Fig. 4a. Not surprisingly, SSTA variability is of negligible magnitude in the subcritical ENSO mode regime. For μ larger than 0.99, the ENSO mode becomes unstable. The magnitude of SSTA variability gets stronger with increasing μ. Unlike the ENSO mode, the SSTA pattern of the simulated ENSO exhibits significant sensitivity to μ. The maximum SSTA variability is located in the central-eastern (far eastern) Pacific in situations where the ENSO mode is weakly (strongly) unstable. Variability of zonal wind stress anomaly varies with μ in a similar way as SSTA. For a weakly unstable ENSO mode (e.g., μ smaller than 1.06), the maximum zonal wind stress variability is in the western Pacific. There is another local center of zonal wind stress variability in the far eastern Pacific. This local variability center is attributed to the easterly (westerly) response in the eastern Pacific during El Niño (La Niña). As the maximum SSTA variability shifts to the eastern Pacific with a more unstable ENSO mode, the center of zonal wind stress variability shifts eastward as well. The contrasting ENSO behavior between the near-critical and far-supercritical ENSO mode regimes is also evidenced in the power spectral density (PSD) of the Niño-3.4 index (Fig. 4b). Alternative choices of the Niño-3 or Niño-4 index have negligible impact on the following results. In the near-critical regime where the ENSO mode is marginally unstable, the PSD peaks at a frequency of about $0.45\ \mathrm{yr}^{-1}$, which is about the same as the ENSO mode. As μ increases to 1.2, the dominant frequency depicted by the maximum PSD is about $0.3\ \mathrm{yr}^{-1}$, which significantly deviates from the ENSO mode's frequency as denoted by the green circles in Fig. 4b. Note that PSD does not smoothly vary with μ but exhibits a more complex behavior as μ increases. A few drastic changes in PSD along varying μ suggest that the ENSO behavior undergoes various stages, which are discussed in detail as follows:

(i) For μ between 0.99 and 1.06, the spatial and temporal characteristics of the simulated ENSO resemble that associated with the ENSO mode. The dominant frequency of the Niño-3.4 index is close to the ENSO mode's frequency (Fig. 4b). The SSTA centroid longitude associated with simulated El Niño events nearly coincides with that of the ENSO mode as well (Fig. 4c). With increasing μ, the dominant frequency gradually becomes smaller (Fig. 4b). The slight deviation of the dominant frequency from that of the ENSO mode may result from the nonlinear correction effect in the weakly unstable regime as noted in Jin (1997). A weak secondary spectral peak is identified at about twice the dominant frequency. This secondary peak corresponds to the second harmonic of the dominant frequency and results from ENSO's nonlinear self-interaction. Physically, this harmonic component is related to the El Niño/La Niña asymmetry. The ENSO behavior at a typical case with $\mu = 1.05$ is presented in Figs. 5a and 6a. As shown by the time evolution of the Niño-3.4 index (Fig. 5a) and equatorial SSTA (Fig. 6a), the coupled system sustains a regular ENSO cycle that is mixed CP/EP-like. The corresponding ENSO orbit, depicted by the trajectory in the Niño-3.4 index-zonal mean equatorial thermocline fluctuation (H_m) phase space, features a single closed loop. The nearly in-quadrature relationship between the Niño-3.4 index and H_m is consistent with the discharge/recharge paradigm for ENSO.

(ii) For μ between 1.07 and 1.11, strong SSTA variability extends to the eastern Pacific rather than being confined to the central-eastern Pacific (Fig. 4a). The dominant frequency of the Niño-3.4 index is about $0.36\ \mathrm{yr}^{-1}$(Fig. 4b). Interestingly, there is another spectral peak at a lower frequency of about $0.18\ \mathrm{yr}^{-1}$. By noticing that the frequency of this spectral peak is half of the dominant frequency, we can speculate that the simulated ENSO undergoes a period-doubling bifurcation as μ crosses 1.07. To examine this possibility, we present the ENSO behavior in a typical case with $\mu = 1.08$ in Figs. 5b and 6b. The phase space trajectory in Fig. 5b clearly demonstrates that the single ENSO orbit observed with μ smaller than 1.07 splits into two interlocked orbits in this case. Starting from any ENSO state, the ENSO cycle regularly travels along these two orbits before returning to the starting point. The time evolution of equatorial SSTA for this case is shown in Fig. 6b. Both CP and EP ENSO are identified, with the former and latter corresponding to the inner and outer ENSO orbit, respectively. The coexistence of two types of El Niño explains the two peaks in the PDF of the SSTA centroid longitude shown in Fig. 4c. In addition, these two types of ENSO alternate regularly, making them exhibit equal occurrences (Fig. 4d). A comparison between the inner ENSO orbit shown in Fig. 5b and the single orbit shown in Fig. 5a indicates that they qualitatively resemble each other. There is a phase shift between them attributed to the fact that the Niño-3.4 index and zonal mean thermocline fluctuation shown in Fig. 5 are anomalies about their long-term average, which exhibit differences among simulations. If the long-term averaged state variables are not removed prior to analysis, the ENSO orbit with $\mu = 1.05$ is close to the inner ENSO orbit with $\mu = 1.08$ except for a slight difference in size. The El Niño patterns associated with these two orbits are close to each other, and both exhibit maximum SSTA in the central-eastern Pacific (not shown). By observing that such an El Niño pattern resembles the SSTA pattern at the peak phase of the ENSO mode, we speculate that both the mixed CP/EP El Niño simulated with $\mu = 1.05$ and the CP-type El Niño simulated with $\mu = 1.08$ essentially represent an ENSO mode subject to quasi-linear or weakly

Brought to you by University of Hawaii at Manoa, Library | Unauthenticated | Downloaded 10/03/23 09:00 AM UTC

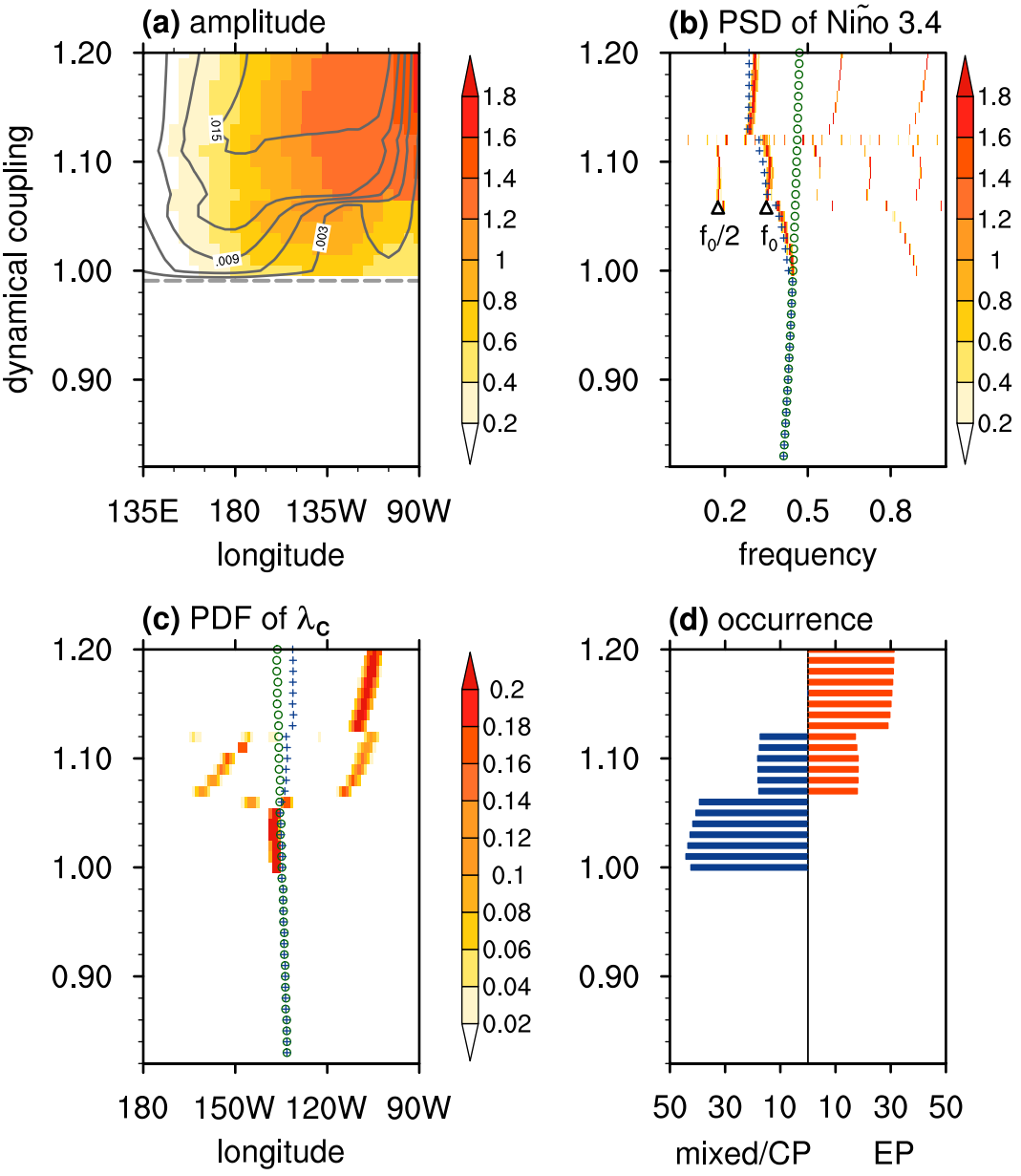

FIG. 4. Dependence of the (a) standard deviation of equatorial SSTA (shaded; °C) and zonal wind stress anomaly (contour; N m^{-2}; contour level: 0.003 N m^{-2}), (b) logarithmic power spectral density (PSD; shaded) of the Niño-3.4 index, (c) PDF of the SSTA centroid longitude associated with El Niño, and (d) number of El Niño occurrences in the mixed/CP group (blue bar) and EP group (red bar) per 100 years on the dynamical coupling coefficient. In (a), the horizontal dashed line marks the critical dynamical coupling coefficient at which the ENSO mode is neutral. In (b), the horizontal axis is the frequency (yr^{-1}). The green circles and blue crosses mark the frequency of the ENSO mode obtained with the observed basic state and the ENSO-rectified basic state in long-term simulations, respectively. See the text in section 4 for the definition of ENSO-rectified basic state. The two triangles mark the frequencies at $f_0/2$ and f_0, with $f_0 = 0.36\ yr^{-1}$. The green circles and blue crosses in (c) are similar to those in (b) but mark the centroid longitude of SSTA at the warm peak phase associated with the ENSO mode. The simulations are subject to an annual mean basic state, and stochastic forcing is switched off.

nonlinear dynamics. Although these two types of El Niño exhibit some pattern difference as shown in Figs. 6a and 6b, they are subject to the same dynamics. The difference between their patterns is due to the fact that they are defined as anomalies to different reference states. The EP El Niño simulated with $\mu = 1.08$, on the other hand, can be understood as a highly distorted ENSO mode subject to strongly nonlinear dynamics. It should be noted that in

Brought to you by University of Hawaii at Manoa, Library | Unauthenticated | Downloaded 10/03/23 09:00 AM UTC

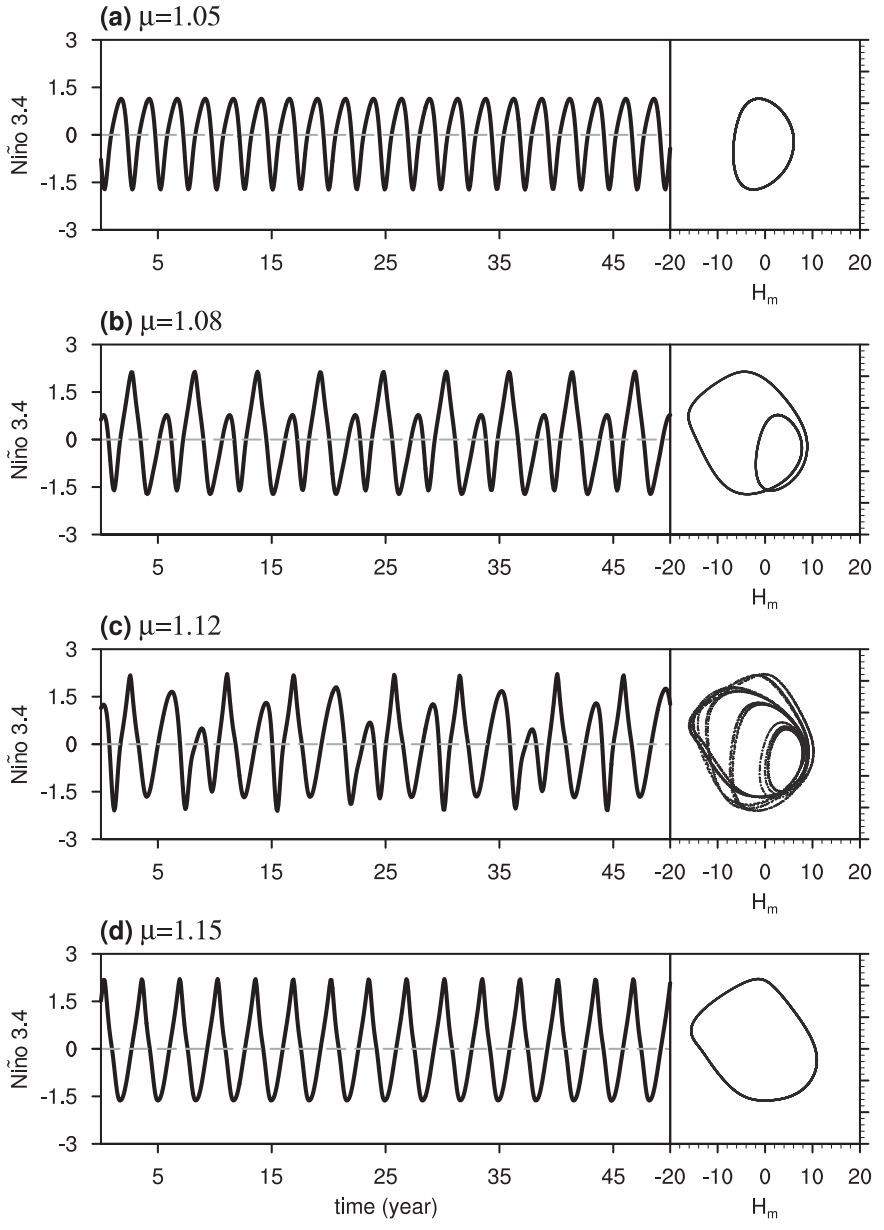

FIG. 5. (a) Shown at left is the 50-yr time series of the Niño-3.4 index (°C) and at right the phase space trajectory plot comprising scatters of the 300-yr Niño-3.4 index and zonal mean equatorial (5°S–5°N average) thermocline fluctuation (H_m; m) in a simulation where the dynamical coupling coefficient is 1.05. (b)–(d) As in (a), but with the dynamical coupling coefficient at 1.08, 1.12, and 1.15, respectively. The simulations are subject to an annual mean basic state, and stochastic forcing is switched off.

general cases where realistic ENSO diversity is simulated, such as the simulations discussed in section 2, both mixed CP/EP and CP El Niño can also be identified without removing the long-term average. This suggests CP El Niño may also be subject to local dynamical processes directly driven by WWBs, which needs further investigation.

(iii) As μ further increases to 1.12, the simulated ENSO becomes aperiodic and exhibits irregular behavior (Fig. 5c). The two ENSO orbits observed with slightly smaller μ further split into more distinct orbits. This ENSO irregularity is also reflected in the broad power spectrum of Niño-3.4 index (Fig. 4c) and irregular occurrences of CP and EP ENSO (Fig. 6c). To explore how this chaotic ENSO behavior emerges, we focus on the range of μ around 1.12. Specifically, a series of simulations with μ varying from 1.11 to 1.13 with an increment of 0.001 is performed. The PSD of

Brought to you by University of Hawaii at Manoa, Library | Unauthenticated | Downloaded 10/03/23 09:00 AM UTC

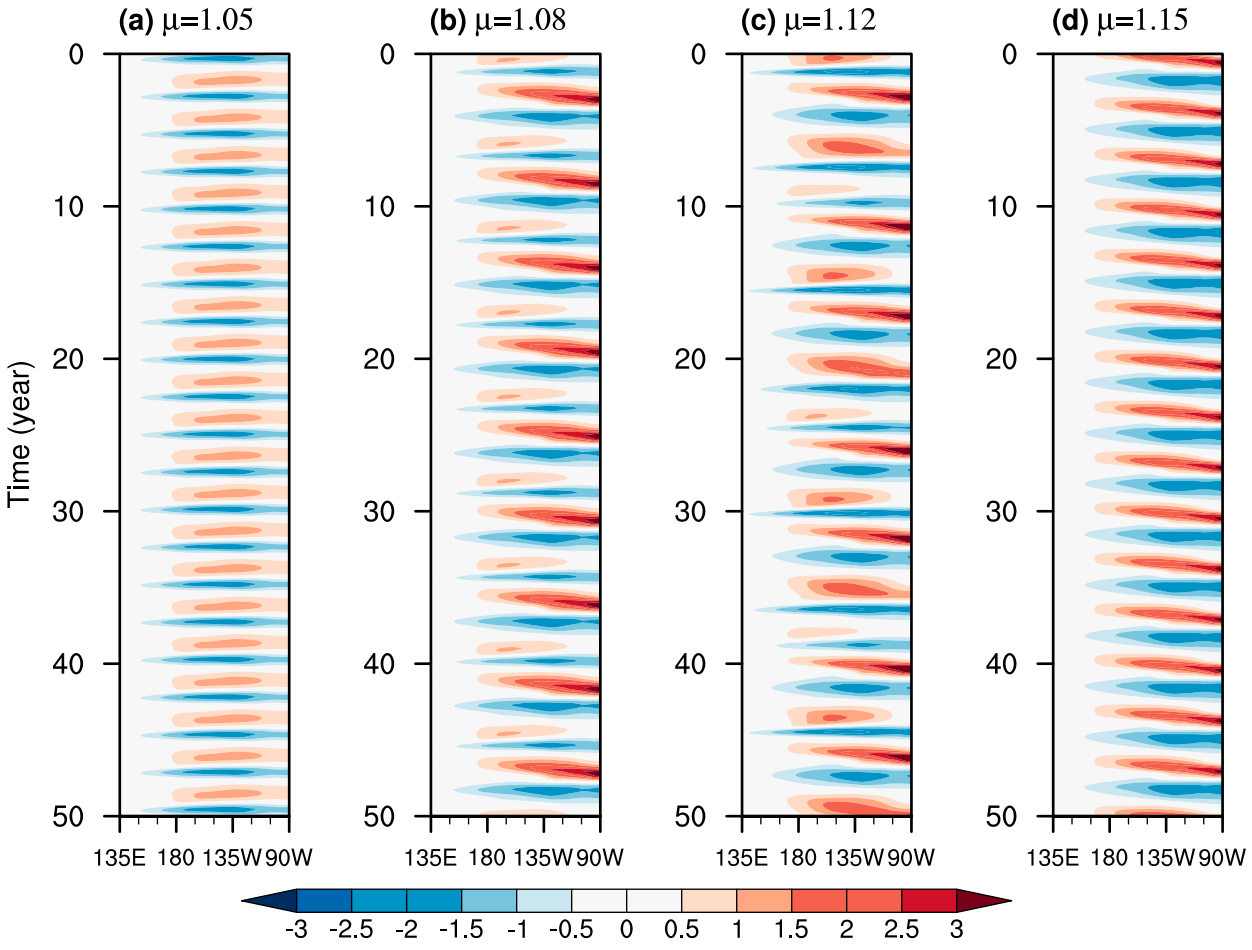

FIG. 6. 50-yr time evolution of equatorial SSTA (°C) in the simulations where the dynamical coupling coefficient is (a) 1.05, (b) 1.08, (c) 1.12, and (d) 1.15. The simulations are subject to an annual mean basic state, and stochastic forcing is switched off.

the Niño-3.4 index in some typical simulations with different μ is shown in Fig. 7. As μ increases from 1.111 to 1.115, a sequence of period doubling, also known as a period-doubling cascade, is clearly identified. The spectral peaks corresponding to these doubled periods are labeled with fractions of the dominant frequency f_0 in each subplot. The other discrete spectral peaks represent subharmonics of these doubled periods resulting from their nonlinear interactions. This period-doubling cascade eventually leads to chaotic ENSO behavior at larger μ, for example, at $\mu = 1.118$. As μ increases further, the broad power spectrum gradually gives its way to discrete spectral peaks again, which will be discussed next.

(iv) For μ larger than 1.13, a regular oscillation of the Niño-3.4 index and a single ENSO orbit in a typical case with $\mu = 1.15$ indicate that the nonlinear coupled system sustains a stable limit cycle (Fig. 5d). Regular EP ENSO occurrences are identified (Fig. 6d). This kind of ENSO behavior explains the existence of a dominant spectral peak at 0.3 yr^{-1} along with its harmonics (Fig. 4b) and a single peak of SSTA centroid longitude in the EP region (Fig. 4c).

As can be seen from the above analysis, the ENSO behavior depends sensitively on the stability of the ENSO mode. With relatively small μ, the ENSO mode is near-neutral or weakly unstable, and the nonlinearity effect is relatively weak. The simulated ENSO resides in the weakly nonlinear regime as the ENSO behavior resembles that of the ENSO mode in terms of the frequency and SSTA pattern. With a sufficiently large μ, the ENSO mode is strongly unstable, making the coupled system subject to a strong nonlinearity effect. In this strongly nonlinear regime, the coupled system sustains a stable EP ENSO-like nonlinear oscillation. Both CP and EP El Niño are captured within the in-between range of μ, which is also referred to as the diversity regime. The coexistence of both types of El Niño clearly demonstrates that deterministic nonlinear processes are sufficient to lead to ENSO diversity. It is important to note, however, that realistic ENSO diversity with irregular occurrences of the two types of El Niño can only be simulated within a tiny range of μ. In addition, ENSO diversity is not reproduced under the observed climate condition where the ENSO mode is near-neutral (i.e., μ being close to 1 in the current model setting).

Brought to you by University of Hawaii at Manoa, Library | Unauthenticated | Downloaded 10/03/23 09:00 AM UTC

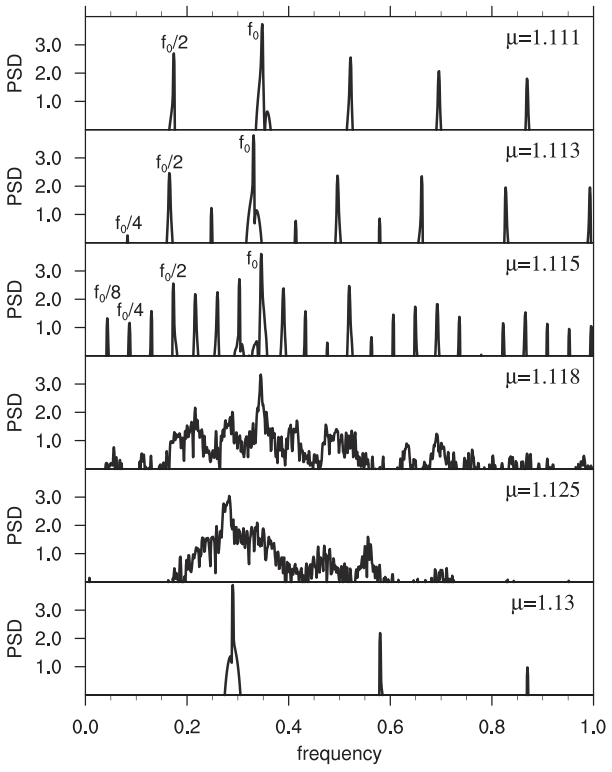

FIG. 7. The PSD of the Niño-3.4 index in simulations with different dynamical coupling coefficients. For each simulation, the corresponding dynamical coupling coefficient is noted in the top-right corner. The simulations are subject to an annual-mean basic state, and stochastic forcing is switched off.

b. *Role of ENSO–seasonal cycle interaction*

All the above analysis is based on simulations with an annual mean basic state. Previous studies clearly illustrated the importance of the climatological seasonal cycle in ENSO's temporal complexity (Jin et al. 1994, 1996; Stuecker et al. 2013, 2015; Chen and Jin 2020). Here, we examine how the seasonal cycle in the basic state influences RCZ-simulated ENSO behavior, particularly ENSO diversity. More specifically, similar simulations as above but with a seasonally varying basic state are performed. To focus on the effects of deterministic nonlinearity, stochastic forcing is kept switched off. As shown in Fig. 8a, finite-amplitude SSTA variability is identified in the subcritical regime of the ENSO mode. This may be attributed to an unstable ENSO mode with boreal summer basic state (see Fig. 4b in Part I). The ENSO behavior shows similar sensitivity to the stability of the ENSO mode as observed with an annual mean basic state. The three regimes of ENSO behavior noted previously are identified as follows:

(i) With relatively small μ (i.e., smaller than 1.03), for example, at $\mu = 1$, the simulated ENSO features regular mixed CP/EP El Niño occurrences (Fig. 9a). Correspondingly, there is a single peak in the PDF of SSTA centroid longitude (Fig. 8c). This ENSO behavior is thus classified as residing in the weakly nonlinear regime noted before with an annual mean basic state. Interestingly, the dominant frequency within this range of μ exactly equals 0.5 yr^{-1} and does not change with μ (Fig. 8b). This phenomenon, named frequency-locking, results from the subharmonic resonance between ENSO and the seasonal cycle, which means that ENSO's frequency is locked to the so-called "Arnold tongues" at rational fractions of the annual frequency. Within this range of μ, the original frequency at about 0.45 yr^{-1} (see Fig. 4b) is entrained to a nearby Arnold tongue at 1/2 of the annual frequency.

(ii) With μ larger than 1.18, the simulated El Niño events are all EP-like (Fig. 9d), suggesting the nature of this regime of ENSO behavior as the strongly nonlinear regime. The dominant frequency of ENSO, which is about 0.3 yr^{-1} in simulations with an annual mean basic state, is entrained and locked to 1/3 of the annual frequency (Fig. 8b). This is again attributed to ENSO's subharmonic resonance with the seasonal cycle. There is another peak in the PSD of the Niño-3.4 index with a slightly smaller power at 2/3 yr^{-1}. This secondary peak can be interpreted as a combination tone between the dominant ENSO frequency and annual frequency.

(iii) The in-between range of μ from 1.04 to 1.17 corresponds to a diversity regime of ENSO as both CP and EP El Niño events can be identified (Figs. 8c,d). In addition, the relative occurrence of the two types of El Niño events varies with μ. More specifically, CP (EP) El Niño sees less (more) frequent occurrences as μ increases. Compared with its counterpart with an annual mean basic state, the ENSO behavior in the current situation exhibits two extinct features. First, irregular occurrences of CP and EP El Niño are universal in this diversity regime. An example of this ENSO irregularity is provided in the equatorial SSTA time evolution in the simulation where $\mu = 1.05$ (Fig. 9b). Note that with an annual mean basic state, the two types of El Niño regularly alternate at this value of μ (Fig. 6b). Second, as can be speculated from a comparison between Figs. 8d and 4d, ENSO diversity is observed in a larger range of μ in this situation than that with an annual mean basic state. An example of ENSO diversity at $\mu = 1.15$, where there is no ENSO diversity with an annual mean basic state, is provided in Fig. 9c. Both of the above two features are related to the fact that the existence of the basic state seasonal cycle favors a chaotic nature of ENSO. Previous studies (e.g., Jin et al. 1994; Tziperman et al. 1994) demonstrated that the ENSO-seasonal cycle interaction leads to chaotic ENSO behavior through the overlapping of frequency-locked subharmonic resonances. This route to chaos is identified in our simulations as well (Fig. 10). As μ decreases from 1.2 to 1.15, the ENSO behavior experiences a so-called "devil's staircase" route from periodic to chaotic. More specifically, at $\mu = 1.18$, the ENSO frequency is discretized into multiple Arnold tongues at 1/6, 1/3, 1/2, 3/3, and 5/6 of the annual frequency, which contrasts with the two spectral peaks in the simulation where $\mu = 1.2$. At $\mu = 1.17$, more Arnold

Brought to you by University of Hawaii at Manoa, Library | Unauthenticated | Downloaded 10/03/23 09:00 AM UTC

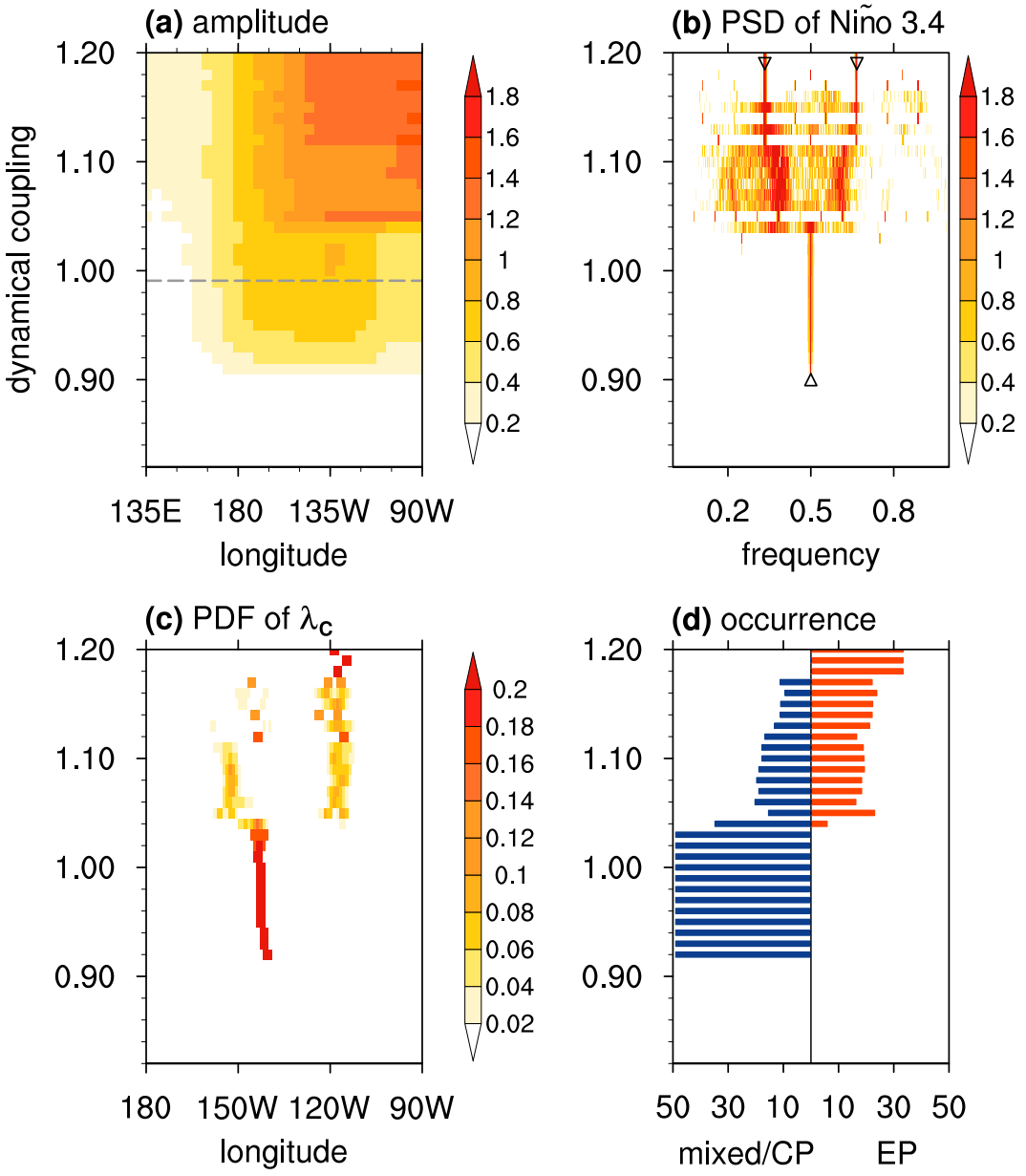

FIG. 8. As in Fig. 4, but for the simulations with a seasonally varying basic state. In (b), the triangle marks the frequency at 1/2 yr^{-1}, and the reverse triangles at 1/3 and 2/3 yr^{-1}.

tongues at another sequence of fractions of the annual frequency are identified. As μ further decreases, the PSD of the Niño-3.4 index generally tends to exhibit a broad spectrum that suggests the overlapping of Arnold tongues, although discrete spectral peaks can still be identified for a few values of μ such as 1.14 and 1.12. Both the multiple discrete spectral peaks and the broad spectrum indicate chaotic ENSO behavior. It should be noted that the aforementioned period-doubling mechanism for ENSO diversity still takes effect with the presence of a seasonally varying basic state. For μ between 1.04 and 1.12, the dominant frequency of ENSO is about 3/8 of the annual frequency, another Arnold tongue of the seasonal cycle. At a lower frequency, a PSD with a weak center close to half of the dominant frequency is identified as well, which is in support of the period-doubling mechanism. Another spectral peak at 5/8 yr^{-1} represents a combination tone between the dominant ENSO frequency and the annual frequency. Compared with that shown in Fig. 4b, PSD is more smoothly dependent on frequency throughout this range of μ (Fig. 8b). This is because the intertwining of the period-doubling cascade and the ENSO's subharmonic resonance with the seasonal cycle efficiently contributes to ENSO irregularity.

Brought to you by University of Hawaii at Manoa, Library | Unauthenticated | Downloaded 10/03/23 09:00 AM UTC

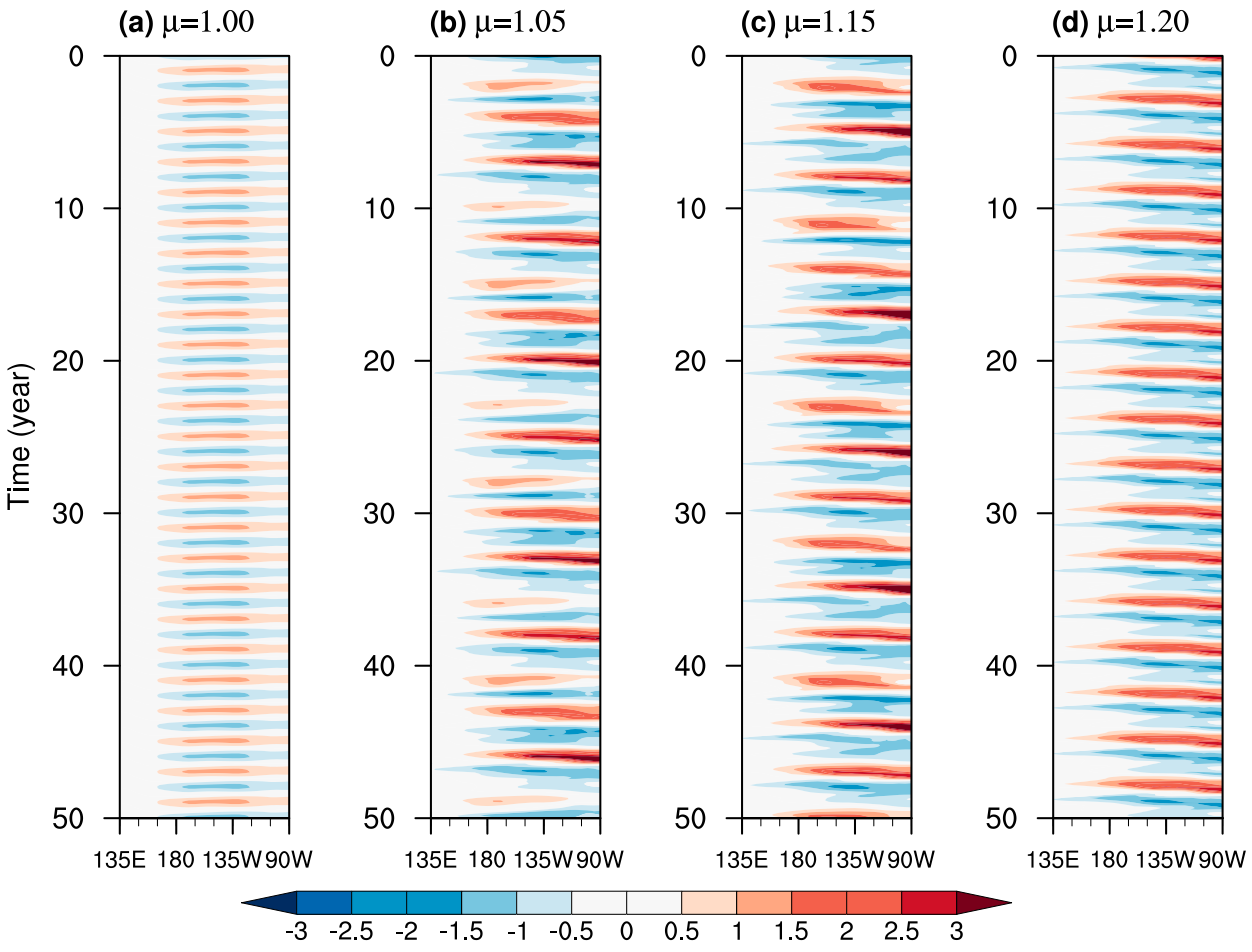

FIG. 9. 50-yr time evolution of equatorial SSTA (°C) in simulations where the dynamical coupling coefficient is (a) 1.0, (b) 1.05, (c) 1.15, and (d) 1.2. The simulations are subject to a seasonally varying basic state, and stochastic forcing is switched off.

c. *Role of stochastic forcing*

In the previous subsections, we demonstrated the essential role of deterministic nonlinearity for ENSO diversity. However, the picture is incomplete because ENSO diversity does not exist in simulations with a default value of μ. In this subsection, we explore how stochastic forcing further contributes to ENSO diversity. This is technically realized via performing simulations as above but with the inclusion of stochastic forcing.

The ENSO behavior in a series of stochastic simulations with varying μ is shown in Fig. 11. The prescribed basic state includes a seasonal cycle. As shown in Figs. 11a and 11b, finite-amplitude SSTA is observed in simulations where μ is smaller than 0.9, in contrast to that shown in Fig. 8. Within this range of μ, the ENSO activity is primarily initiated and sustained by stochastic forcing. The simulated ENSO events exhibit features resembling the ENSO mode and are mixed CP/EP-like. Irregular ENSO occurrences are identified in this situation (not shown). Such ENSO irregularity induced by stochastic forcing in the stable ENSO regime was also noted by Chang et al. (1996). The more frequent occurrences of El Niño events with increasing μ are due to the fact that a less stable coupled system allows more ENSO events with an amplitude that exceeds the threshold to take place. At the large end of μ, the SSTA variability shown in Fig. 11a resembles that shown in Fig. 8a, indicating that the effect of stochastic forcing on energizing ENSO activity saturates when the coupled system is strongly nonlinear. An important implication from Fig. 11 is that the diversity regime originally identified in Fig. 8 is further broadened, especially toward the lower end of μ. ENSO diversity is identified with μ larger than 0.96 rather than 1.04 as in the deterministic simulations. This explains why multiple ENSO flavors are captured in the stochastic simulation with a default value of μ as shown in Fig. 1a. The effect of stochastic forcing on broadening the diversity regime can also be identified in the simulations with an annual mean basic state (Fig. 12). The range of diversity μ seeing multiple types of ENSO is between 1.07 and 1.12 in the deterministic simulations (Fig. 4d) but expands significantly toward both ends of μ in the stochastic simulations (Fig. 12d).

Another salient difference between the deterministic and stochastic simulations is that, upon incorporating stochastic

Brought to you by University of Hawaii at Manoa, Library | Unauthenticated | Downloaded 10/03/23 09:00 AM UTC

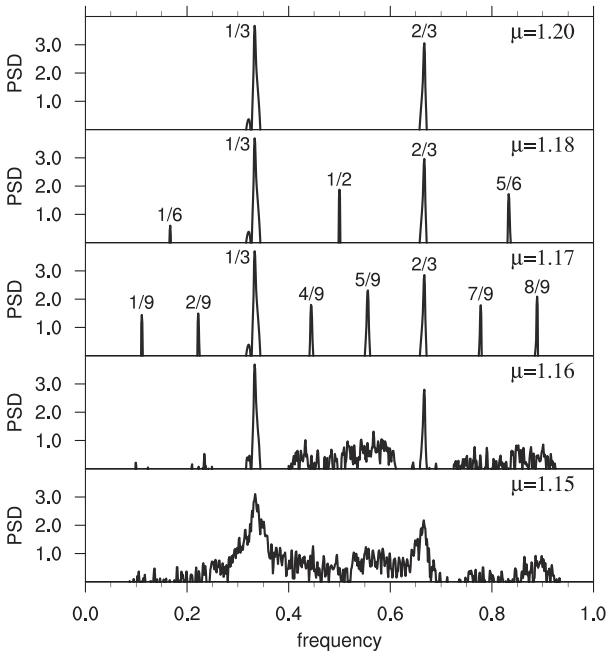

FIG. 10. As in Fig. 7, but for the simulations subject to a seasonally varying basic state. Each fraction number denotes the frequency of the corresponding spectral peak.

forcing, the discrete PSD peaks in Figs. 4b and 8b, originally identified in the deterministic simulations, are smoothed and replaced by a relatively broad power spectrum centering around the dominant frequency (Figs. 11b and 12b). The harmonic components that manifested as spectral peaks at multiples of the dominant frequency, especially those shown in Fig. 4b, are no longer observable. This smearing effect induced by stochastic forcing was also noted by Chang et al. (1996), Wang et al. (1999), and Jin et al. (2020). However, it is interesting to note that a secondary spectral peak still exists across the diversity regime and the strongly nonlinear regime in the stochastic simulations with a seasonally varying basic state. As discussed previously, this secondary spectral peak with a relatively high frequency represents a combination tone of ENSO and the seasonal cycle. It is related to the double-dip La Niña following EP El Niño, a phenomenon only observed with a seasonally varying basic state.

To better illustrate the effect of stochastic forcing, we examine how the ENSO behavior changes with varying intensities of stochastic forcing. This is realized via performing a series of simulations in which the nondimensional parameter controlling the intensity of stochastic forcing I_{stc} increases from 0 to 2 with an increment of 0.1. As shown in Fig. 13, the simulated ENSO is dominated by mixed/CP El Niño when stochastic forcing is weak. However, more EP El Niño occurrences are identified with a stronger intensity of stochastic forcing. This result confirms our finding that stochastic forcing favors ENSO diversity. It also has implications for the effect of state-dependent noise. Previous observational studies suggested that WWBs are modulated by the underlying SST associated with ENSO (Eisenman et al. 2005; Tziperman and Yu 2007; Seiki and Takayabu 2007; Puy et al. 2016). More frequent occurrences or stronger intensity of WWBs during El Niño are expected to efficiently excite EP El Niño and thus favor ENSO diversity, which is consistent with Chen et al. (2015).

4. Relationship among the climate mean state, ENSO activity, and ENSO diversity

Previous observational studies revealed a relationship between the climate mean state (or low-frequency climate variability) and intensity of ENSO variability (e.g., Jin et al. 2003; Rodgers et al. 2004; Yeh and Kirtman 2004). A connection between the mean state and preferred ENSO flavor was also identified in climate model simulations (e.g., Choi et al. 2011, 2012). In this section, we examine whether such a mean state–ENSO relationship is observed in RCZ simulations.

A nonlinear simulation with an anomaly model such as RCZ is typically accompanied by a climate drift manifested as nonzero long-term averaged state variables, especially in situations where the nonlinearity effect is significant. The climate drift pattern associated with the simulation under the observed climate condition is shown in Fig. 14a. It features a slightly warmer cold tongue and cooler warm pool compared with the observations. Corresponding to this decreased mean zonal temperature gradient, a weakened Walker circulation and a deepened (shoaled) thermocline in the eastern (western) Pacific can be identified. How the equatorial SST drift depends on μ, or equivalently on ENSO mode stability, is shown in Fig. 15. In all three sets of simulations, the SST drift gets stronger with increasing μ. As discussed in section 3, the ENSO behavior exhibits similar dependence on μ as well. More specifically, as μ increases, ENSO exhibits stronger activity as evidenced by the larger amplitude of SSTA variability, and EP (CP) El Niño sees more (less) frequent occurrences. This result indicates a possible relationship between the mean state and ENSO behavior in RCZ. To further test this hypothesis, we examine if this relationship applies on a decadal-to-multidecadal time scale using the simulation with default model settings. In the following discussion, decadal variability indicates variability on and above the decadal time scale.

After removing the climate drift, a 20-yr running average is applied to the model variables to capture the mean state decadal variability. The first empirical orthogonal function (EOF) mode of the SST decadal variability, of which the explained variance reaches 83%, exhibits maximum SSTA in the eastern Pacific (Fig. 14b). Accordingly, we use a mean state index $\tilde{T}_{EP}$, defined as the 20-yr running averaged SSTA over the Niño-3 region, to quantify the mean state decadal variability. The mean state index can also be defined as the 20-yr running averaged SSTA over the eastern Pacific minus that over the western Pacific. As this alternative index shows a high correlation coefficient (0.98) with $\tilde{T}_{EP}$, the latter is chosen for simplicity. We also define three ENSO indices to quantify the decadal variability of ENSO behavior. The first two ENSO indices are the standard deviation and skewness of the Niño-3.4 index in the 20-yr running window. These two indices measure the decadal variation of ENSO activity and

Brought to you by University of Hawaii at Manoa, Library | Unauthenticated | Downloaded 10/03/23 09:00 AM UTC

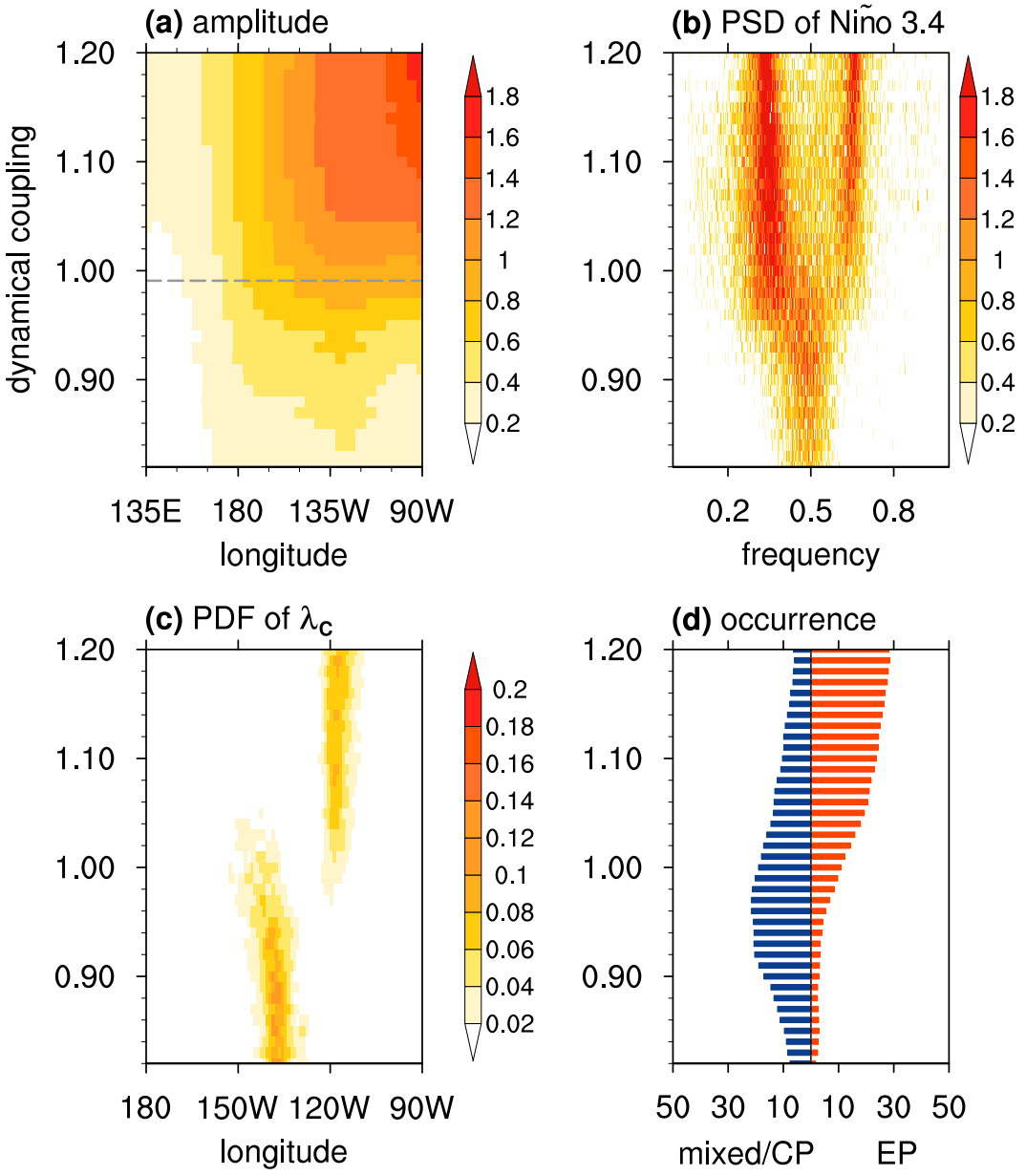

FIG. 11. As in Fig. 4, but for the simulations with a seasonally varying basic state and driven by stochastic forcing.

ENSO asymmetry, respectively. The skewness is calculated following An and Jin (2004). The third ENSO index is the ENSO flavor index. It is defined as $(N_{EP} - N_{CP})/(N_{EP} + N_{CP})$, where N_{EP} and N_{CP} are the EP and CP El Niño occurrences within the running window, respectively. In situations where this index is close to 1 (−1), EP (CP) El Niño is preferred over CP (EP) El Niño. A comparison between the time series of the mean state index $\tilde{T}_{EP}$ and three ENSO indices is shown in Fig. 16. There is a close relationship between the mean state index and all three ENSO indices. The correlation coefficients all reach the 99.99% significance level. During epochs with cold tongue warming, or equivalently weakened mean zonal temperature gradient, ENSO exhibits stronger variability. In addition, EP (CP) El Niño sees more (less) frequent occurrences. The covariation of ENSO activity and preferred ENSO flavor can be understood by recalling that EP El Niño is of stronger amplitude than CP El Niño. EP El Niño being more favored also explains the stronger positive skewness of the Niño-3.4 index because El Niño–La Niña asymmetry is more evident during EP El Niño than CP El Niño. The above results clearly confirm that the close relationship among the mean state, ENSO activity, and ENSO diversity identified with the climate drift can be observed on the decadal time scale as well.

Previous studies suggested that the mean state–ENSO relationship may result from ENSO's nonlinear rectification effect

Brought to you by University of Hawaii at Manoa, Library | Unauthenticated | Downloaded 10/03/23 09:00 AM UTC

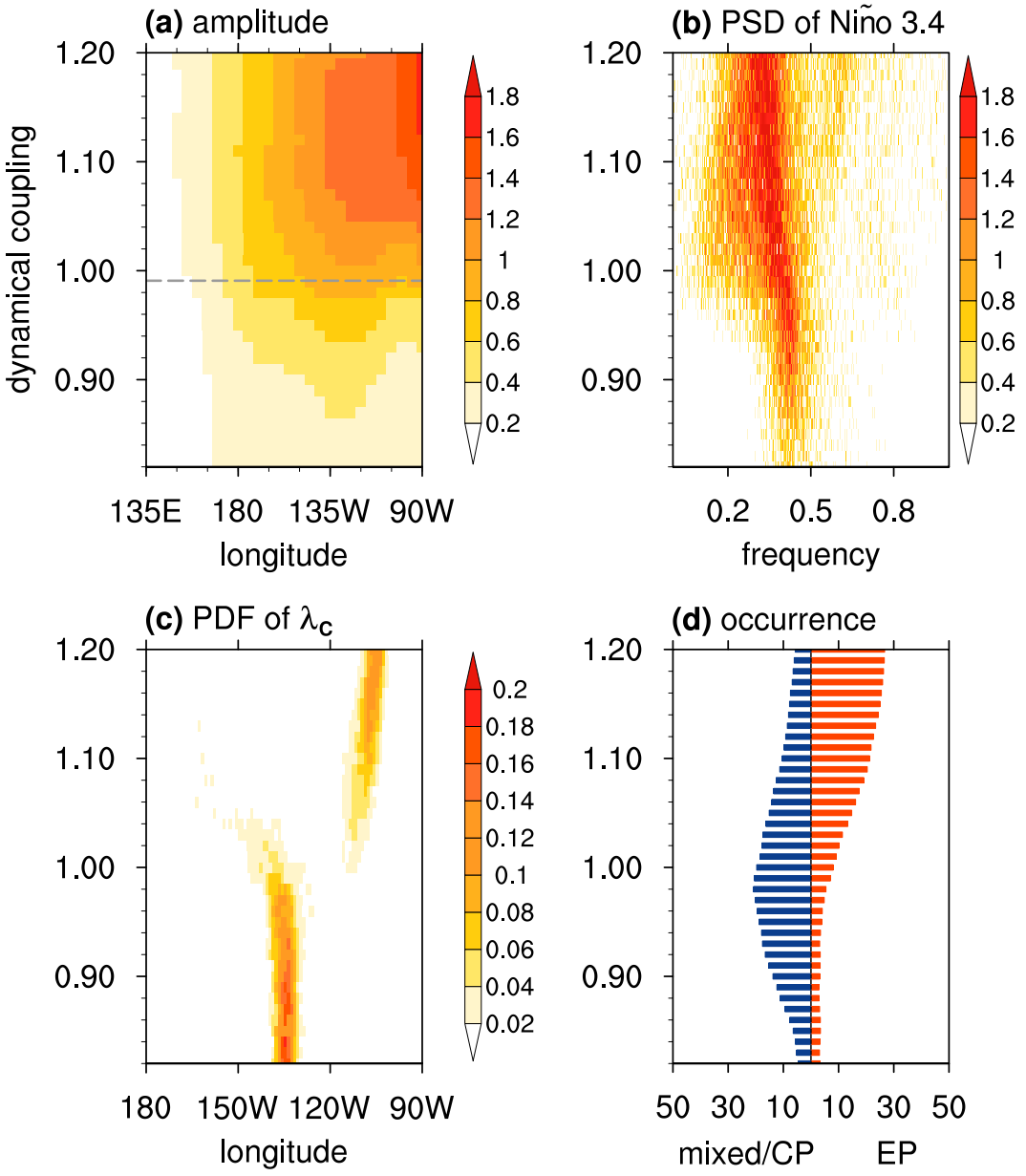

FIG. 12. As in Fig. 4, but for the simulations with an annual mean basic state and driven by stochastic forcing.

on the mean state associated with El Niño–La Niña asymmetry on the one hand (e.g., Rodgers et al. 2004; Choi et al. 2009, 2012; Liu et al. 2022), and from the climate mean state's control of ENSO properties on the other hand (Choi et al. 2009, 2011). As shown in Fig. 15, the mean state index is about in phase with the ENSO indices. A lead–lag correlation coefficient exhibits maximum correlation at a zero lead/lag. Thus, it is difficult to separate the two-way interaction between the mean state and ENSO. However, ENSO behavior being modulated by the mean state can indeed be identified in our analysis. For example, the phenomenon of a cold tongue warming being accompanied by more EP El Niño occurrences may be understood from the perspective that a weakened mean zonal temperature gradient is inducive to a more EP-like ENSO mode (see Part I). To better illustrate this, we perform linear stability analyses with the ENSO-rectified basic state associated with simulations presented in section 3a and examine if the ENSO mode properties are consistent with long-term simulated ENSO behavior. The ENSO-rectified basic state is obtained by superposing the climate drift onto the originally prescribed basic state. As shown in Fig. 4b, the frequency of the ENSO mode corresponding to the ENSO-rectified basic state, denoted by blue crosses, matches well with the dominant spectral peak in the nonlinear long-term simulation across different ENSO regimes. In addition, in the strongly nonlinear regime where EP El Niño is dominant, the SSTA

Brought to you by University of Hawaii at Manoa, Library | Unauthenticated | Downloaded 10/03/23 09:00 AM UTC

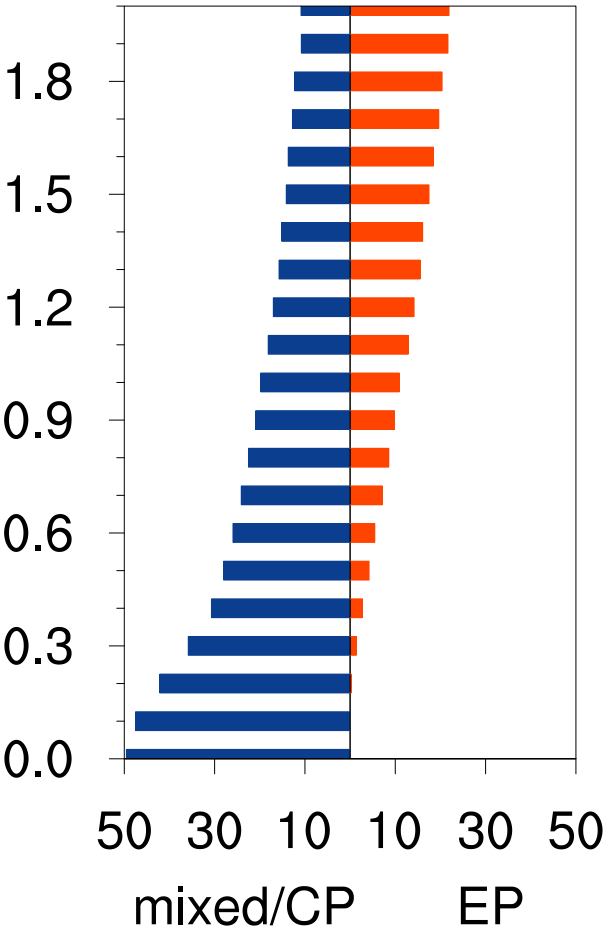

FIG. 13. The number of El Niño occurrences in the mixed/CP group (blue bar) and EP group (red bar) per 100 years in simulations where the relative amplitude of stochastic forcing I_{stc} increases from 0 to 2 with an increment of 0.1. The simulations are subject to a seasonally varying basic state.

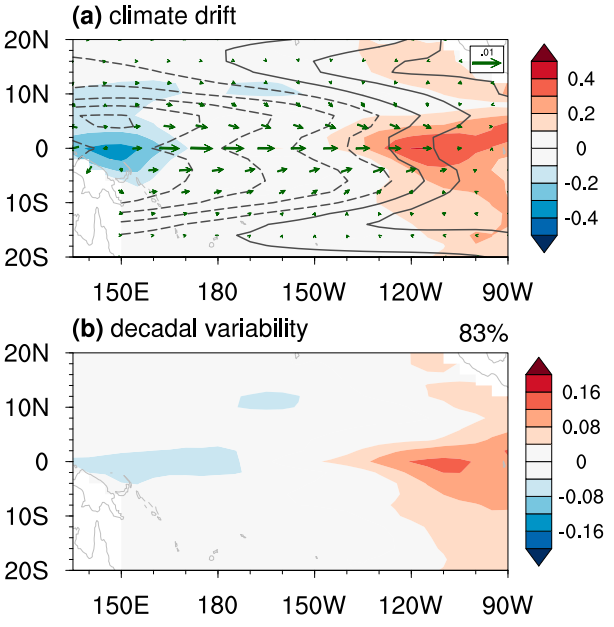

FIG. 14. (a) 1000-yr averaged SSTA (shaded; °C), thermocline depth (contour; m), and surface wind stress (vector; N m^{-2}) in the stochastic simulation with a seasonally varying basic state and default model parameters. (b) The first EOF mode of SSTA decadal variability. See the text on how the decadal variability is defined. The explained variance of this mode is indicated at the top right of the figure.

centroid longitude associated with the ENSO mode shifts slightly eastward once the climate drift is included in the basic state (Fig. 4c). However, there is a significant discrepancy in SSTA centroid longitude between the simulated ENSO and the ENSO mode. The above features demonstrate that ENSO's rectification effect on the mean state is relevant to the change in ENSO behavior across different regimes. However, this linear argument is insufficient to fully explain the dominance of EP El Niño in the strongly nonlinear regime, especially in terms of the spatial pattern. It is thus speculated that EP El Niño is strongly subject to nonlinear dynamics. The mean state's control on ENSO diversity is also evidenced by the finding that dependence of the preferred ENSO flavor on climate conditions generally resembles that of the ENSO mode, which is solely determined by the prescribed climate condition. Inspired by Part I, we examined ENSO diversity in a two-dimensional parameter space spanned by varying intensities of the zonal advective feedback and thermocline feedback. As demonstrated in Part I, the ENSO mode exhibits more CP-like and EP-like features with stronger zonal advective feedback and thermocline feedback, respectively (see Fig. 11 in Part I). Consistent with that, more frequent occurrences of El Niño in the mixed/CP group and EP group are observed at the strong end of zonal advective feedback and thermocline feedback, respectively (Fig. 17). Note that the EP El Niño does not exist when the ENSO mode is strongly stable (i.e., both the two feedbacks see weak intensities). The lack of ENSO diversity in this situation is consistent with our findings discussed in the previous section.

5. Summary and discussions

Under the observed climate condition, realistic ENSO diversity characterized by irregular occurrences of CP and EP El Niño is successfully captured in long-term RCZ simulations with either a seasonally varying or an annual mean basic state. Some interesting features of ENSO pattern diversity and temporal complexity are identified in these simulations. The background seasonal cycle is found to play an important role in the El Niño–La Niña duration asymmetry, particularly the emergence of multiyear La Niña. The relevant physical process involved merits further investigation.

As demonstrated in Part I of this two-part study, there is a single leading ENSO mode under the observed climate condition. How this ENSO mode leads to the coexistence of CP and EP El Niño is investigated in this paper. By systematically exploring the ENSO behavior across the subcritical-to-supercritical regime

Brought to you by University of Hawaii at Manoa, Library | Unauthenticated | Downloaded 10/03/23 09:00 AM UTC

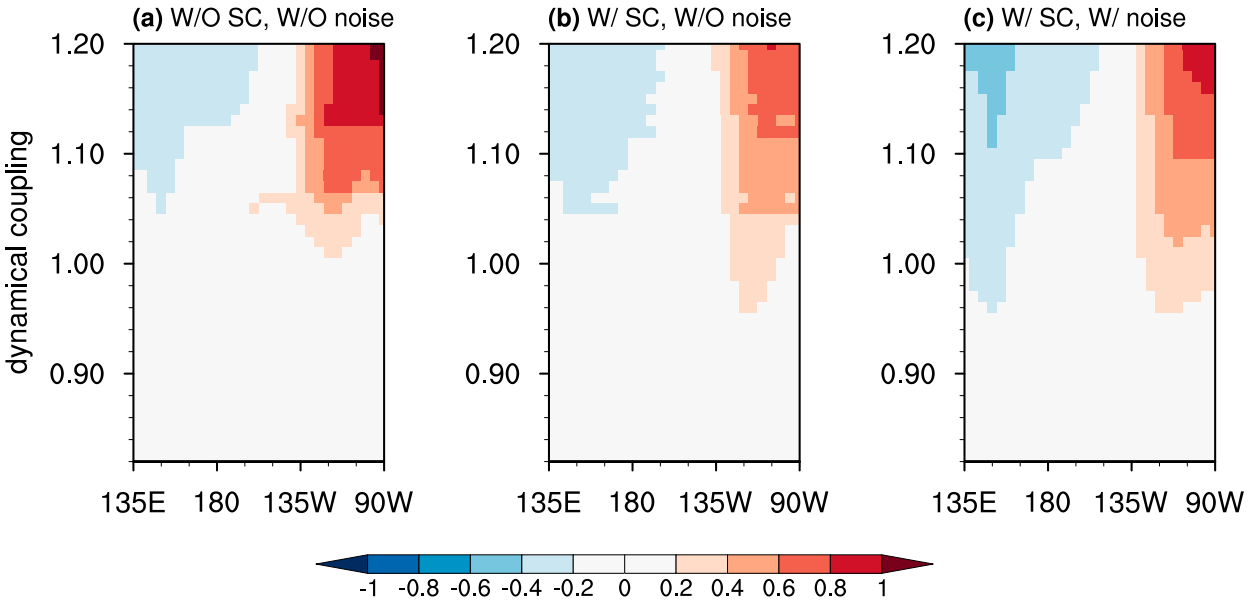

FIG. 15. Dependence of 1000-yr averaged equatorial SSTA (°C) on dynamical coupling coefficient in simulations (a) with an annual mean basic state and without stochastic forcing, (b) with a seasonally varying basic state and without stochastic forcing, and (c) with a seasonally varying basic state and with stochastic forcing.

for the ENSO mode, we propose a nonlinear pathway from ENSO mode toward ENSO diversity. A schematic diagram of this mechanism is provided in Fig. 18.

The ENSO behavior in long-term simulations is sensitively dependent on the stability of the ENSO mode, which determines the intensity of the nonlinearity effect of the coupled system. Stochastic forcing is another important factor determining ENSO behavior. Without stochastic forcing, the coupled system sustains a limit cycle solution when the ENSO mode is weakly unstable. This limit cycle solution exhibits ENSO mode-like spatiotemporal characteristics. In contrast, regular EP ENSO events are identified when the ENSO mode becomes strongly unstable. ENSO diversity is observed within the in-between range of ENSO mode stability. Two nonlinear routes to chaos are relevant to the emergence of ENSO diversity within this range. As the ENSO mode becomes increasingly unstable starting from being near-neutral or weakly unstable, the single ENSO orbit experiences a period-doubling bifurcation and splits into coexisting CP-like and EP-like orbits. With an annual mean basic state, the two types of ENSO regularly alternate within a relatively narrow range of ENSO mode stability near moderately unstable. Near the upper bound of this range, the period-doubling cascade results in chaotic ENSO behavior featuring irregular occurrences of CP and EP ENSO. With a seasonally varying basic state, the overlapping subharmonic resonances between ENSO and the seasonal cycle allow ENSO irregularity and diversity to occur within a wider range of ENSO mode stability. Both the period-doubling and subharmonic resonance route to chaos were proposed to explain ENSO irregularity in previous studies (Münnich et al. 1991; Jin et al. 1994; Tziperman et al. 1994). In this paper, we further demonstrate that they are also relevant for ENSO diversity. In addition to these two deterministic routes to chaos, stochastic forcing functions as another source of ENSO irregularity and diversity. Once stochastic forcing is included, the range of ENSO mode stability seeing ENSO diversity is broadened toward both ends. This explains the existence of ENSO diversity under the observed climate condition where the ENSO mode is near-neutral.

Note that the diversity regime occurs within a relatively small range of the ENSO mode stability, even with the presence of stochastic processes. Either a too-stable or too-unstable ENSO mode precludes ENSO diversity. Such a relatively narrow diversity regime may have important implications for why state-of-the-art climate models generally have difficulties capturing ENSO diversity to a satisfying degree. A diagnosis of the ENSO mode's stability in climate models and how it is related to the model performance in simulating ENSO diversity will be investigated in a future study. It needs to be pointed out that the dynamical coupling and thermal damping exhibit a cancellation effect on ENSO activity (Lloyd et al. 2009). It deserves further investigation whether the range of diversity regime can be broadened if this cancellation effect is considered.

Our findings in this study clearly demonstrate the importance of nonlinear dynamics for EP El Niño. This finding supports the argument by Takahashi et al. (2011) that EP El Niño is essentially an extreme manifestation of the ENSO phenomenon. Without stochastic forcing, EP El Niño can only be simulated when the ENSO mode is unstable. Self-growth of the unstable ENSO mode leads to a finite-amplitude ENSO oscillation and kick-starts the nonlinear processes. When the ENSO mode is stable or near-neutral, finite-amplitude stochastic forcing effectively initiates the nonlinear processes. Identification of the most relevant nonlinear processes for ENSO diversity is beyond

Brought to you by University of Hawaii at Manoa, Library | Unauthenticated | Downloaded 10/03/23 09:00 AM UTC

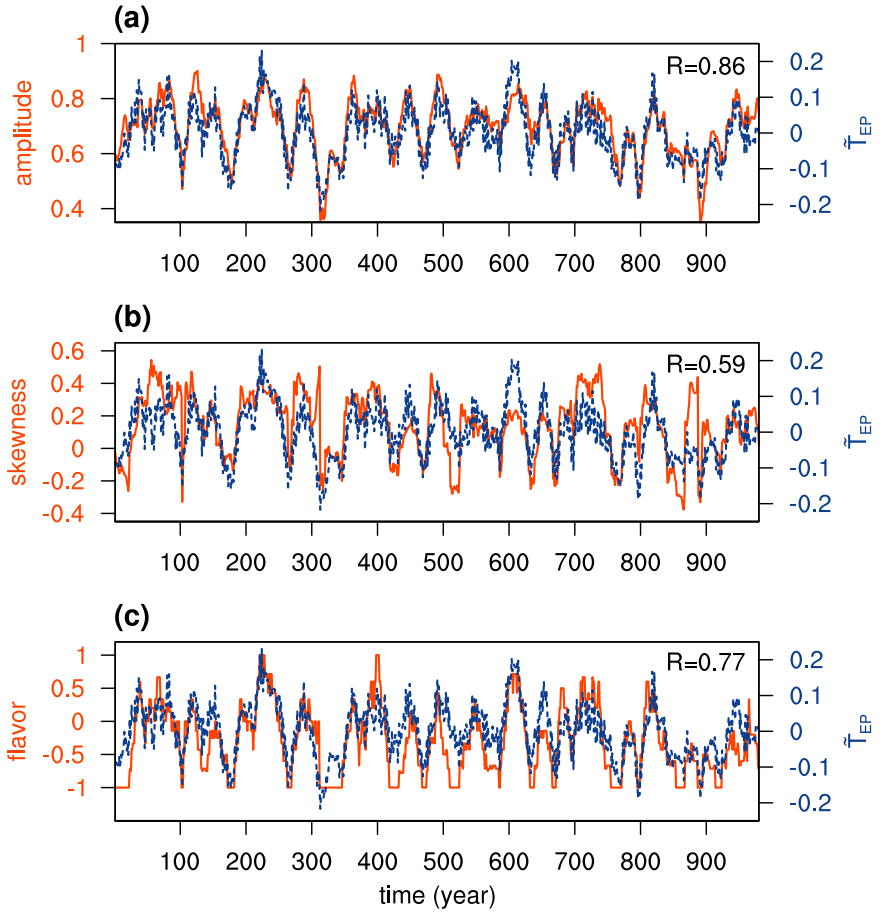

FIG. 16. (a) Time series of the amplitude of Niño-3.4 index (solid red line; °C) and time-averaged SSTA over the Niño-3 region (dashed blue line; °C) in the 20-yr running window. (b) As in (a), but with the red line denoting the skewness of the Niño-3.4 index in the 20-yr running window. (c) As in (a), but with the red line denoting the ENSO flavor index. See the text for the definition of the ENSO flavor index. All the indices are calculated from the stochastically driven simulation with a seasonally varying basic state default model parameters. In each plot, the correlation coefficient between the red and blue lines is noted in the top-right corner.

the scope of this study. Here, we briefly discuss the effect of atmospheric nonlinearity, which was suggested to play a key role in ENSO diversity in previous studies (Williams and Patricola 2018; Okumura 2019; Geng et al. 2020). We performed a long-term stochastic simulation with the nonlinear atmospheric processes switched off. This is technically realized through (i) removing the nonlinear terms (i.e., quadratic and cubic terms) in the convective heating parameterization (see section 3 in Part I) and (ii) removing the state-dependent part of WWB. The result (not shown) indicates that ENSO diversity identified in simulations discussed in previous sections becomes much less evident once atmospheric nonlinearity is switched off. Instead, the simulated ENSO features irregular occurrences of the ENSO mode-like events in these simulations. This finding indicates that the atmospheric nonlinear processes may indeed facilitate ENSO diversity. Whether and how oceanic nonlinear processes (e.g., nonlinear dynamical heating and nonlinear subsurface temperature response to thermocline fluctuation) contribute to ENSO diversity simulated with RCZ will be explored in a future study. With a more comprehensive model, we can further investigate the effect of other nonlinear processes, such as ENSO-tropical instability wave (TIW) interaction, on ENSO diversity.

Even though a nonlinear pathway toward ENSO diversity has been put forth using a Cane–Zebiak-type framework in the present study, we would like to point out that the possibility of linear dynamics contributing to ENSO diversity cannot be ruled out. As we mentioned in Part I, whether there exists more than one ENSO mode in a framework resolving more physical processes relevant to ENSO diversity still needs to be explored. Therefore, the fundamental dynamics of ENSO diversity merits further investigation with a more comprehensive theoretical framework.

In this study, a close relationship among the climate mean state, ENSO activity, and ENSO diversity is identified. Such a relationship results from a two-way interaction between the

Brought to you by University of Hawaii at Manoa, Library | Unauthenticated | Downloaded 10/03/23 09:00 AM UTC

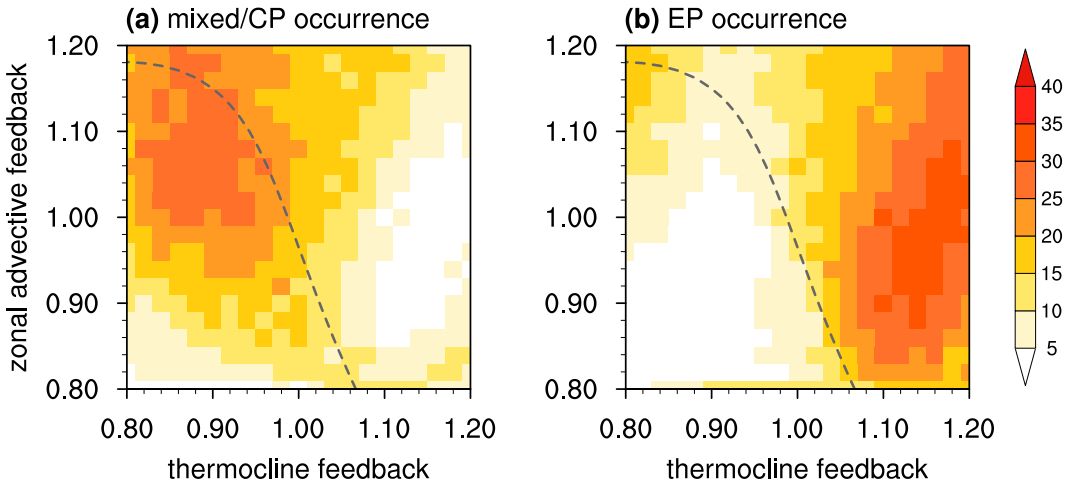

FIG. 17. Dependence of the number of El Niño occurrences per 100 years in the (a) mixed/CP group and (b) EP group on the intensity of zonal advective feedback and thermocline feedback. The dashed curve denotes a zero-growth rate contour of the ENSO mode. The ENSO mode has a negative (positive) growth rate to the left and bottom (right and top) of the zero-growth rate contour.

mean state and ENSO. A weakened mean zonal temperature gradient is shown to be accompanied by a stronger intensity of ENSO variability and more (fewer) occurrences of EP (CP) El Niño. The relationship between the mean zonal temperature gradient and ENSO activity has also been noted in previous research. Some studies support the relationship between a weakened mean zonal temperature gradient and a stronger ENSO activity on the decadal-to-multidecadal time scale or vice versa (e.g., Yeh and Kirtman 2004; Burgman et al. 2008; Ogata et al. 2013; Okumura et al. 2017; An et al. 2018; Hu and Fedorov 2018; Wyman et al. 2020). However, a recent study by Callahan et al. (2021) found that climate models robustly project a decreased ENSO activity with a weakened mean zonal temperature gradient on the millennium time scale. Therefore, the direction of this ENSO activity–mean zonal temperature gradient relationship, especially how it depends on the time scale of climate variability, still needs to be further studied. In contrast to the ENSO activity–mean state relationship, the correlation between ENSO activity and ENSO diversity was not widely studied previously. Consistent with our findings, an observation analysis by Sun and Yu (2009) suggested that El Niño tends to be located in the EP (CP) region during epochs when ENSO activity is strong (weak). Whether such a correlation can be identified during the observed shift of preferred ENSO type, such as around the late 1970s and the early 2000s, is an interesting topic for further study.

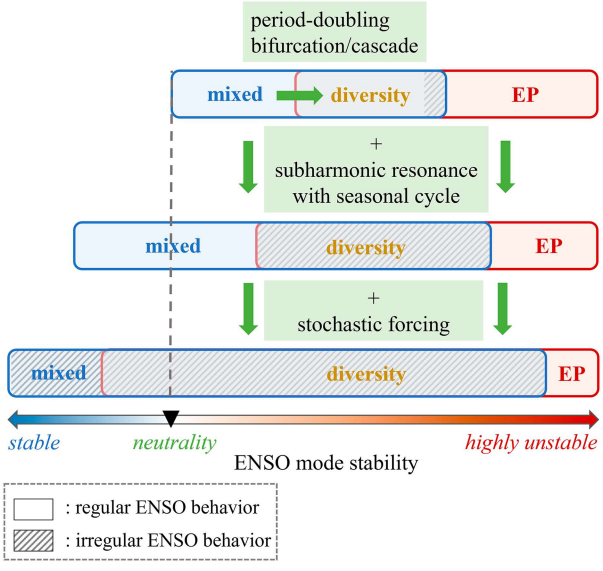

FIG. 18. Schematic diagram of the nonlinear mechanism for ENSO diversity.

The tropical Pacific decadal variability identified in this study may exclusively result from the intrinsic mean state–ENSO interaction. It may also be initiated by the decadal component of stochastic forcing and then sustained by the mean state–ENSO interaction. To test which of the two pathways is more relevant, we may simply force the model with a high-frequency-only stochastic forcing and examine whether the decadal variability still exists. The decadal variability in nature may also arise from low-frequency forcing external to the tropical Pacific climate system, such as Atlantic multidecadal oscillation, the solar cycle, volcano activities, and anthropogenic forcing (Power et al. 2021, and references therein). Whether the internal dynamics or external forcing is more relevant to decadal variability has not been fully addressed (Fedorov et al. 2020). With RCZ, we may be able to compare the relevance of these two processes by individually tuning the intensity of mean state–ENSO interaction (e.g., via tuning model parameters to control the intensity or preferred flavor of ENSO) and prescribed low-frequency external forcing.

Acknowledgments. This research was supported by the U.S. National Science Foundation (AGS-2219257). All the model

Brought to you by University of Hawaii at Manoa, Library | Unauthenticated | Downloaded 10/03/23 09:00 AM UTC

simulations were performed on the University of Hawaii High-Performance Computing (UH-HPC) cluster. We thank three anonymous reviewers for providing valuable comments and suggestions. Thanks also go to May Izumi for editing the manuscript. This is SOEST contribution 11726.

Data availability statement. The reanalysis data for deriving the model's basic state are openly available from the Asia-Pacific Data-Research Center at http://apdrc.soest.hawaii.edu/data/data.php and from the NOAA Physical Sciences Laboratory at https://psl.noaa.gov/data/gridded/index.html. The model simulation data and derived data for analysis are available upon request to the corresponding author.

REFERENCES

An, S.-I., and F.-F. Jin, 2004: Nonlinearity and asymmetry of ENSO. *J. Climate*, **17**, 2399–2412, https://doi.org/10.1175/1520-0442(2004)017<2399:NAAOE>2.0.CO;2.

——, S.-H. Im, and S.-Y. Jun, 2018: Changes in ENSO activity during the last 6,000 years modulated by background climate state. *Geophys. Res. Lett.*, **45**, 2467–2475, https://doi.org/10.1002/2017GL076250.

Bejarano, L., and F.-F. Jin, 2008: Coexistence of equatorial coupled modes of ENSO. *J. Climate*, **21**, 3051–3067, https://doi.org/10.1175/2007JCLI1679.1.

Burgman, R. J., P. S. Schopf, and B. P. Kirtman, 2008: Decadal modulation of ENSO in a hybrid coupled model. *J. Climate*, **21**, 5482–5500, https://doi.org/10.1175/2008JCLI1933.1.

Callahan, C. W., C. Chen, M. Rugenstein, J. Bloch-Johnson, S. Yang, and E. J. Moyer, 2021: Robust decrease in El Niño/Southern Oscillation amplitude under long-term warming. *Nat. Climate Change*, **11**, 752–757, https://doi.org/10.1038/s41558-021-01099-2.

Capotondi, A., 2013: ENSO diversity in the NCAR CCSM4 climate model. *J. Geophys. Res. Oceans*, **118**, 4755–4770, https://doi.org/10.1002/jgrc.20335.

——, and P. D. Sardeshmukh, 2015: Optimal precursors of different types of ENSO events. *Geophys. Res. Lett.*, **42**, 9952–9960, https://doi.org/10.1002/2015GL066171.

——, and Coauthors, 2015: Understanding ENSO diversity. *Bull. Amer. Meteor. Soc.*, **96**, 921–938, https://doi.org/10.1175/BAMS-D-13-00117.1.

Chang, P., L. Ji, H. Li, and M. Flügel, 1996: Chaotic dynamics versus stochastic processes in El Niño-Southern Oscillation in coupled ocean-atmosphere models. *Physica D*, **98**, 301–320, https://doi.org/10.1016/0167-2789(96)00116-9.

Chen, D., and Coauthors, 2015: Strong influence of westerly wind bursts on El Niño diversity. *Nat. Geosci.*, **8**, 339–345, https://doi.org/10.1038/ngeo2399.

Chen, H.-C., and F.-F. Jin, 2020: Fundamental behavior of ENSO phase locking. *J. Climate*, **33**, 1953–1968, https://doi.org/10.1175/JCLI-D-19-0264.1.

Chen, M., T. Li, X. Shen, and B. Wu, 2016: Relative roles of dynamic and thermodynamic processes in causing evolution asymmetry between El Niño and La Niña. *J. Climate*, **29**, 2201–2220, https://doi.org/10.1175/JCLI-D-15-0547.1.

Chen, N., and A. J. Majda, 2017: Simple stochastic dynamical models capturing the statistical diversity of El Niño Southern Oscillation. *Proc. Natl. Acad. Sci. USA*, **114**, 1468–1473, https://doi.org/10.1073/pnas.1620766114.

——, ——, and S. Thual, 2018: Observations and mechanisms of a simple stochastic dynamical model capturing El Niño diversity. *J. Climate*, **31**, 449–471, https://doi.org/10.1175/JCLI-D-16-0880.1.

Choi, J., S.-I. An, B. Dewitte, and W. W. Hsieh, 2009: Interactive feedback between the tropical Pacific decadal oscillation and ENSO in a coupled general circulation model. *J. Climate*, **22**, 6597–6611, https://doi.org/10.1175/2009JCLI2782.1.

——, ——, J.-S. Kug, and S.-W. Yeh, 2011: The role of mean state on changes in El Niño's flavor. *Climate Dyn.*, **37**, 1205–1215, https://doi.org/10.1007/s00382-010-0912-1.

——, ——, and S.-W. Yeh, 2012: Decadal amplitude modulation of two types of ENSO and its relationship with the mean state. *Climate Dyn.*, **38**, 2631–2644, https://doi.org/10.1007/s00382-011-1186-y.

Chung, P.-H., and T. Li, 2013: Interdecadal relationship between the mean state and El Niño types. *J. Climate*, **26**, 361–379, https://doi.org/10.1175/JCLI-D-12-00106.1.

DiNezio, P. N., and C. Deser, 2014: Nonlinear controls on the persistence of La Niña. *J. Climate*, **27**, 7335–7355, https://doi.org/10.1175/JCLI-D-14-00033.1.

Eisenman, I., L. Yu, and E. Tziperman, 2005: Westerly wind bursts: ENSO's tail rather than the dog? *J. Climate*, **18**, 5224–5238, https://doi.org/10.1175/JCLI3588.1.

Fedorov, A. V., S. Hu, A. T. Wittenberg, A. F. Z. Levine, and C. Deser, 2020: ENSO low-frequency modulation and mean state interactions. *El Niño Southern Oscillation in a Changing Climate*, Amer. Geophys. Union, 173–198, https://doi.org/10.1002/9781119548164.ch8.

Freund, M. B., B. J. Henley, D. J. Karoly, H. V. McGregor, N. J. Abram, and D. Dommenget, 2019: Higher frequency of Central Pacific El Niño events in recent decades relative to past centuries. *Nat. Geosci.*, **12**, 450–455, https://doi.org/10.1038/s41561-019-0353-3.

Geng, L., and F.-F. Jin, 2022: ENSO diversity simulated in a revised Cane-Zebiak model. *Front. Earth Sci.*, **10**, 899323, https://doi.org/10.3389/feart.2022.899323.

——, and ——, 2023: Insights into ENSO diversity from an intermediate coupled model. Part I: Uniqueness and sensitivity of the ENSO mode. *J Climate*, **36**, 7509–7525, https://doi.org/10.1175/JCLI-D-23-0043.1.

Geng, T., W. Cai, and L. Wu, 2020: Two types of ENSO varying in tandem facilitated by nonlinear atmospheric convection. *Geophys. Res. Lett.*, **47**, e2020GL088784, https://doi.org/10.1029/2020GL088784.

Graham, N. E., and T. P. Barnett, 1987: Sea surface temperature, surface wind divergence, and convection over tropical oceans. *Science*, **238**, 657–659, https://doi.org/10.1126/science.238.4827.657.

Hayashi, M., and M. Watanabe, 2017: ENSO complexity induced by state dependence of westerly wind events. *J. Climate*, **30**, 3401–3420, https://doi.org/10.1175/JCLI-D-16-0406.1.

Hu, S., and A. V. Fedorov, 2018: Cross-equatorial winds control El Niño diversity and change. *Nat. Climate Change*, **8**, 798–802, https://doi.org/10.1038/s41558-018-0248-0.

Iwakiri, T., and M. Watanabe, 2021: Mechanisms linking multiyear La Niña with preceding strong El Niño. *Sci. Rep.*, **11**, 17465, https://doi.org/10.1038/s41598-021-96056-6.

Jin, F.-F., 1997: An equatorial ocean recharge paradigm for ENSO. Part I: Conceptual model. *J. Atmos. Sci.*, **54**, 811–829, https://doi.org/10.1175/1520-0469(1997)054<0811:AEORPF>2.0.CO;2.

Brought to you by University of Hawaii at Manoa, Library | Unauthenticated | Downloaded 10/03/23 09:00 AM UTC

——, J. D. Neelin, and M. Ghil, 1994: El Niño on the devil's staircase: Annual subharmonic steps to chaos. *Science*, **264**, 70–72, https://doi.org/10.1126/science.264.5155.70.

——, ——, and ——, 1996: El Nino/Southern Oscillation and the annual cycle: Subharmonic frequency-locking and aperiodicity. *Physica D*, **98**, 442–465, https://doi.org/10.1016/0167-2789(96)00111-X.

——, S.-I. An, A. Timmermann, and J. Zhao, 2003: Strong El Niño events and nonlinear dynamical heating. *Geophys. Res. Lett.*, **30**, 1120, https://doi.org/10.1029/2002GL016356.

——, H.-C. Chen, S. Zhao, M. Hayashi, C. Karamperidou, M. F. Stuecker, R. Xie, and L. Geng, 2020: Simple ENSO models. *El Niño Southern Oscillation in a Changing Climate*, Amer. Geophys. Union, 119–151, https://doi.org/10.1002/9781119548164.ch6.

Kang, I.-S., and J.-S. Kug, 2002: El Niño and La Niña sea surface temperature anomalies: Asymmetry characteristics associated with their wind stress anomalies. *J. Geophys. Res.*, **107**, 4372, https://doi.org/10.1029/2001JD000393.

Kug, J.-S., and Y.-G. Ham, 2011: Are there two types of La Nina? *Geophys. Res. Lett.*, **38**, L16704, https://doi.org/10.1029/2011GL048237.

——, F.-F. Jin, and S.-I. An, 2009: Two types of El Niño events: Cold tongue El Niño and warm pool El Niño. *J. Climate*, **22**, 1499–1515, https://doi.org/10.1175/2008JCLI2624.1.

——, J. Choi, S.-I. An, F.-F. Jin, and A. T. Wittenberg, 2010: Warm pool and cold tongue El Niño events as simulated by the GFDL 2.1 coupled GCM. *J. Climate*, **23**, 1226–1239, https://doi.org/10.1175/2009JCLI3293.1.

Lee, T., and M. J. McPhaden, 2010: Increasing intensity of El Niño in the central-equatorial Pacific. *Geophys. Res. Lett.*, **37**, L14603, https://doi.org/10.1029/2010GL044007.

Liu, C., W. Zhang, F.-F. Jin, M. F. Stuecker, and L. Geng, 2022: Equatorial origin of the observed tropical Pacific quasi-decadal variability from ENSO nonlinearity. *Geophys. Res. Lett.*, **49**, e2022GL097903, https://doi.org/doi:10.1029/2022GL097903.

Lloyd, J., E. Guilyardi, H. Weller, and J. Slingo, 2009: The role of atmosphere feedbacks during ENSO in the CMIP3 models. *Atmos. Sci. Lett.*, **10**, 170–176, https://doi.org/10.1002/asl.227.

McPhaden, M. J., 2012: A 21st century shift in the relationship between ENSO SST and warm water volume anomalies. *Geophys. Res. Lett.*, **39**, L09706, https://doi.org/10.1029/2012GL051826.

Münnich, M., M. A. Cane, and S. E. Zebiak, 1991: A study of self-excited oscillations of the tropical ocean–atmosphere system. Part II: Nonlinear cases. *J. Atmos. Sci.*, **48**, 1238–1248, https://doi.org/10.1175/1520-0469(1991)048<1238:ASOSEO>2.0.CO;2.

Newman, M., M. A. Alexander, and J. D. Scott, 2011a: An empirical model of tropical ocean dynamics. *Climate Dyn.*, **37**, 1823–1841, https://doi.org/10.1007/s00382-011-1034-0.

——, S.-I. Shin, and M. A. Alexander, 2011b: Natural variation in ENSO flavors. *Geophys. Res. Lett.*, **38**, L14705, https://doi.org/10.1029/2011GL047658.

Ogata, T., S.-P. Xie, A. Wittenberg, and D.-Z. Sun, 2013: Interdecadal amplitude modulation of El Niño–Southern Oscillation and its impact on tropical Pacific decadal variability. *J. Climate*, **26**, 7280–7297, https://doi.org/10.1175/JCLI-D-12-00415.1.

Ohba, M., and H. Ueda, 2009: Role of nonlinear atmospheric response to SST on the asymmetric transition process of ENSO. *J. Climate*, **22**, 177–192, https://doi.org/10.1175/2008JCLI2334.1.

Okumura, Y. M., 2019: ENSO diversity from an atmospheric perspective. *Curr. Climate Change Rep.*, **5**, 245–257, https://doi.org/10.1007/s40641-019-00138-7.

——, T. Sun, and X. Wu, 2017: Asymmetric modulation of El Niño and La Niña and the linkage to tropical Pacific decadal variability. *J. Climate*, **30**, 4705–4733, https://doi.org/10.1175/JCLI-D-16-0680.1.

Power, S., and Coauthors, 2021: Decadal climate variability in the tropical Pacific: Characteristics, causes, predictability, and prospects. *Science*, **374**, eaay9165, https://doi.org/10.1126/science.aay9165.

Puy, M., J. Vialard, M. Lengaigne, and E. Guilyardi, 2016: Modulation of equatorial Pacific westerly/easterly wind events by the Madden–Julian Oscillation and convectively-coupled Rossby waves. *Climate Dyn.*, **46**, 2155–2178, https://doi.org/10.1007/s00382-015-2695-x.

Ren, H.-L., and F.-F. Jin, 2013: Recharge oscillator mechanisms in two types of ENSO. *J. Climate*, **26**, 6506–6523, https://doi.org/10.1175/JCLI-D-12-00601.1.

Rodgers, K. B., P. Friederichs, and M. Latif, 2004: Tropical Pacific decadal variability and its relation to decadal modulations of ENSO. *J. Climate*, **17**, 3761–3774, https://doi.org/10.1175/1520-0442(2004)017<3761:TPDVAI>2.0.CO;2.

Seiki, A., and Y. N. Takayabu, 2007: Westerly wind bursts and their relationship with intraseasonal variations and ENSO. Part I: Statistics. *Mon. Wea. Rev.*, **135**, 3325–3345, https://doi.org/10.1175/MWR3477.1.

Stuecker, M. F., A. Timmermann, F.-F. Jin, S. McGregor, and H.-L. Ren, 2013: A combination mode of the annual cycle and the El Niño/Southern Oscillation. *Nat. Geosci.*, **6**, 540–544, https://doi.org/10.1038/ngeo1826.

——, F.-F. Jin, and A. Timmermann, 2015: El Niño–Southern Oscillation frequency cascade. *Proc. Natl. Acad. Sci. USA*, **112**, 13 490–13 495, https://doi.org/10.1073/pnas.1508622112.

Su, J., R. Zhang, T. Li, X. Rong, J.-S. Kug, and C.-C. Hong, 2010: Causes of the El Niño and La Niña amplitude asymmetry in the equatorial eastern Pacific. *J. Climate*, **23**, 605–617, https://doi.org/10.1175/2009JCLI2894.1.

Sun, F., and J.-Y. Yu, 2009: A 10–15-yr modulation cycle of ENSO intensity. *J. Climate*, **22**, 1718–1735, https://doi.org/10.1175/2008JCLI2285.1.

Takahashi, K., and B. Dewitte, 2016: Strong and moderate nonlinear El Niño regimes. *Climate Dyn.*, **46**, 1627–1645, https://doi.org/10.1007/s00382-015-2665-3.

——, A. Montecinos, K. Goubanova, and B. Dewitte, 2011: ENSO regimes: Reinterpreting the canonical and Modoki El Niño. *Geophys. Res. Lett.*, **38**, L10704, https://doi.org/10.1029/2011GL047364.

——, C. Karamperidou, and B. Dewitte, 2019: A theoretical model of strong and moderate El Niño regimes. *Climate Dyn.*, **52**, 7477–7493, https://doi.org/10.1007/s00382-018-4100-z.

Taschetto, A. S., A. Sen Gupta, N. C. Jourdain, A. Santoso, C. C. Ummenhofer, and M. H. England, 2014: Cold tongue and warm pool ENSO events in CMIP5: Mean state and future projections. *J. Climate*, **27**, 2861–2885, https://doi.org/10.1175/JCLI-D-13-00437.1.

——, C. C. Ummenhofer, M. F. Stuecker, D. Dommenget, K. Ashok, R. R. Rodrigues, and S.-W. Yeh, 2020: ENSO atmospheric teleconnections. *El Niño Southern Oscillation in a Changing Climate*, Amer. Geophys. Union, 309–335, https://doi.org/10.1002/9781119548164.ch14.

Timmermann, A., F.-F. Jin, and J. Abshagen, 2003: A nonlinear theory for El Niño bursting. *J. Atmos. Sci.*, **60**, 152–165,

Brought to you by University of Hawaii at Manoa, Library | Unauthenticated | Downloaded 10/03/23 09:00 AM UTC

https://doi.org/10.1175/1520-0469(2003)060<0152:ANTFEN>2.0.CO;2.

Tziperman, E., and L. Yu, 2007: Quantifying the dependence of westerly wind bursts on the large-scale tropical Pacific SST. *J. Climate*, **20**, 2760–2768, https://doi.org/10.1175/JCLI4138a.1.

——, L. Stone, M. A. Cane, and H. Jarosh, 1994: El Niño chaos: Overlapping of resonances between the seasonal cycle and the Pacific ocean–atmosphere oscillator. *Science*, **264**, 72–74, https://doi.org/10.1126/science.264.5155.72.

Vimont, D. J., M. A. Alexander, and M. Newman, 2014: Optimal growth of central and east Pacific ENSO events. *Geophys. Res. Lett.*, **41**, 4027–4034, https://doi.org/10.1002/2014GL059997.

——, M. Newman, D. S. Battisti, and S.-I. Shin, 2022: The role of seasonality and the ENSO mode in central and east Pacific ENSO growth and evolution. *J. Climate*, **35**, 3195–3209, https://doi.org/10.1175/JCLI-D-21-0599.1.

Wang, B., A. Barcilon, and Z. Fang, 1999: Stochastic dynamics of El Niño–Southern Oscillation. *J. Atmos. Sci.*, **56**, 5–23, https://doi.org/10.1175/1520-0469(1999)056<0005:SDOENO>2.0.CO;2.

Williams, I. N., and C. M. Patricola, 2018: Diversity of ENSO events unified by convective threshold sea surface temperature: A nonlinear ENSO index. *Geophys. Res. Lett.*, **45**, 9236–9244, https://doi.org/10.1029/2018GL079203.

Wyman, D. A., J. L. Conroy, and C. Karamperidou, 2020: The tropical Pacific ENSO–mean state relationship in climate models over the last millennium. *J. Climate*, **33**, 7539–7551, https://doi.org/10.1175/JCLI-D-19-0673.1.

Xiang, B., B. Wang, and T. Li, 2013: A new paradigm for the predominance of standing central Pacific warming after the late 1990s. *Climate Dyn.*, **41**, 327–340, https://doi.org/10.1007/s00382-012-1427-8.

Xie, R., and F.-F. Jin, 2018: Two leading ENSO modes and El Niño types in the Zebiak–Cane model. *J. Climate*, **31**, 1943–1962, https://doi.org/10.1175/JCLI-D-17-0469.1.

Yang, Q., A. J. Majda, and N. Chen, 2021: ENSO diversity in a tropical stochastic skeleton model for the MJO, El Niño, and dynamic Walker circulation. *J. Climate*, **34**, 3481–3501, https://doi.org/10.1175/JCLI-D-20-0447.1.

Yang, S., Z. Li, J.-Y. Yu, X. Hu, W. Dong, and S. He, 2018: El Niño–Southern Oscillation and its impact in the changing climate. *Natl. Sci. Rev.*, **5**, 840–857, https://doi.org/10.1093/nsr/nwy046.

Yeh, S.-W., and B. P. Kirtman, 2004: Tropical Pacific decadal variability and ENSO amplitude modulation in a CGCM. *J. Geophys. Res.*, **109**, C11009, https://doi.org/10.1029/2004JC002442.

——, J.-S. Kug, and S.-I. An, 2014: Recent progress on two types of El Niño: Observations, dynamics, and future changes. *Asia-Pac. J. Atmos. Sci.*, **50**, 69–81, https://doi.org/10.1007/s13143-014-0028-3.

Zebiak, S. E., and M. A. Cane, 1987: A model El Niño–Southern Oscillation. *Mon. Wea. Rev.*, **115**, 2262–2278, https://doi.org/10.1175/1520-0493(1987)115<2262:AMENO>2.0.CO;2.

Brought to you by University of Hawaii at Manoa, Library | Unauthenticated | Downloaded 10/03/23 09:00 AM UTC